

Aleksey Kochura

**GROWTH, MAGNETIC AND TRANSPORT
PROPERTIES OF InSb AND II-IV-As₂
SEMICONDUCTORS DOPED WITH MANGANESE**

Thesis for degree of Doctor of Philosophy to be presented with due permission
for public examination and criticism in the Auditorium 1383 at Lappeenranta
University of Technology, Lappeenranta, Finland, on the 19th of December
2011, at noon

Acta Universitatis
Lappeenrantaensis 462

Supervisor Prof. Erkki Lähderanta
Department of Mathematics and Physics
Lappeenranta University of Technology
Lappeenranta, Finland

Reviewers Prof. Ernest Arushanov
Institute of Applied Physics,
Academy of Sciences of Moldova Republic
Kishinev, Moldova Republic

Prof. Dr. Hab. Witold Dobrowolski
Institute of Physics
Polish Academy of Sciences
Warszawa, Poland

Opponent Prof. Alexander Granovsky
Magnetism Department
Moscow State University
Moscow, Russia

ISBN 978-952-265-190-7
ISBN 978-952-265-191-4 (PDF)
ISSN 1456-4491

Lappeenrannan teknillinen yliopisto
Digipaino 2011

To my family

Abstract

Aleksey Kochura

Growth, magnetic and transport properties of InSb and II-IV-As₂ semiconductors doped with manganese.

Lappeenranta 2011

62 p.

Acta Universitatis Lappeenrantaensis 462

Diss. Lappeenranta University of Technology

ISBN ISBN 978-952-265-190-7, ISBN 978-952-265-191-4 (PDF), ISSN 1456-4491

This thesis is devoted to growth and investigations of Mn-doped InSb and II-IV-As₂ semiconductors, including Cd_{1-x}Zn_xGeAs₂:Mn, ZnSiAs₂:Mn bulk crystals, ZnSiAs₂:Mn/Si heterostructures.

Bulk crystals were grown by direct melting of starting components followed by fast cooling. Mn-doped ZnSiAs₂/Si heterostructures were grown by vacuum-thermal deposition of ZnAs₂ and Mn layers on Si substrates followed by annealing. The compositional and structural properties of samples were investigated by different methods. The samples consist of micro- and nano- sizes clusters of an additional ferromagnetic Mn-X phases ($X = \text{Sb or As}$).

Influence of magnetic precipitations on magnetic and electrical properties of the investigated materials was examined. With relatively high Mn concentration the main contribution to magnetization of samples is by MnSb or MnAs clusters. These clusters are responsible for high temperature behavior of magnetization and relatively high Curie temperature: up to 350 K for Mn-doped II-IV-As₂ and about 600 K for InMnSb. The low-field magnetic properties of Mn-doped II-IV-As₂ semiconductors and ZnSiAs₂:Mn/Si heterostructures are connected to the nanosize MnAs particles. Also influence of nanosized MnSb clusters on low-field magnetic properties of InMnSb have been observed. The contribution of paramagnetic phase to magnetization rises at low temperatures or in samples with low Mn concentration. Source of this contribution is not only isolated Mn ions, but also small complexes, mainly dimmers and trimmers formed by Mn ions, substituting cation positions in crystal lattice.

Resistivity, magnetoresistance and Hall resistivity properties in bulk Mn-doped II-IV-As₂ and InSb crystals was analyzed. The interaction between delocalized holes and $3d$ shells of the Mn ions together with giant Zeeman splitting near the cluster interface are respond for negative magnetoresistance. Additionally to high temperature critical point the low-temperature ferromagnetic transition was observed Anomalous Hall effect was observed in Mn doped samples and analyzed for InMnSb. It was found that MnX clusters influence significantly on magnetic scattering of carriers.

Keywords: Synthesis of semiconductors, diluted magnetic semiconductors, hybrid magnetic materials, magnetic heterostructures, nanoclusters, galvanomagnetic effects, magnetoresistance, anomalous Hall effect.

UDC 621.315.59:621.313.552.3:539.2:537.621

Acknowledgments

This work was carried out at the Department of Mathematics and Physics of Lappeenranta University of Technology, Finland, in the Wihuri Physical Laboratory at the Department of Physics, University of Turku, Finland, in the Kurnakov Institute of General and Inorganic Chemistry, Russian Academy of Science, Russia and in Kursk State Technical University (at present South-West State University), Russia. Investigations were performed in close cooperation with colleagues from the Ioffe Institute of Russian Academy of Science, St Petersburg, Russia.

I would like to express my sincere gratitude to my supervisor Prof. Erkki Lähderanta for his kind support and attention to my activities. It is my pleasure to thank Prof. Sergey Marenkin for his patient teaching, care and interest to my work. My special gratitude is to Dr. Alexander Lashkul for fruitful collaborations.

I wish to thank Prof. Ernest Arushanov and Prof. Witold Dobrowolski reviewing the thesis.

My sincere gratitude to Prof. Alexander Granovsky as opponent.

I would like to express my gratitude to the Lappeenranta University of Technology for financial aid and for the possibility to complete the work over this thesis. Financial support from the Centre for International Mobility (CIMO) (grant No. TM-06-4408), Russian Foundation for Basic Research (projects No. 07-03-00810, 08-03-90706, 09-03-90743, 10-03-0666), and International Association for Promotion of Co-operation with Scientists from the New Independent States of the former Soviet Union (INTAS) (grant No. 06-1000014-5792) are acknowledged.

Finally, I wish to thank my wife Evgenija and my little daughter Ekaterina for their love and inspiration.

Lappeenranta, 2011

Aleksey Kochura

Contents

Abstract	5
Acknowledgements	7
List of publications	11
List of symbols and abbreviations	13
1 Introduction	15
1.1 Short review and motivation for the research	15
1.2. Outline of the work	17
1.3. Summary of the publications	19
2 Growth and experimental procedure	22
2.1 Synthesis of InSb and (Zn,Cd)(Ge,Si)As ₂ crystals and ZnSiAs ₂ /Si heterostructures doped with manganese	22
2.2 Structural properties of the grown samples	27
2.2.1 Examination of the structure by optical, electron scanning and atomic force microscopy	27
2.2.2 X-ray powder diffraction analyses	30
3 Magnetic properties of InSb and II-IV-As₂ semiconductors doped with Mn	33
3.1 Experimental procedure	33
3.2 Influence of magnetic precipitations on magnetic properties of investigated materials	33
3.2.1 MnAs precipitates in II-IV-As ₂ :Mn	33
3.2.2 MnSb precipitates in InSb	36
3.3 Magnetism of diluted magnetic semiconductor matrix	37
3.4 Nanosize MnAs and MnSb precipitations	43
4 Transport properties of InSb and II-IV-As₂ semiconductors doped with Mn	47
4.1 Experimental procedure	47
4.2 Temperature dependence of resistivity	47
4.3 Magnetoresistivity and low-temperature ferromagnetic ordering	50
4.4 Hall effect	55
5 Conclusions	58
References	59
Original papers	69

List of publications

This thesis is based on the experimental work carried out during 2006-2011.

The following original papers with description of my contribution are included in the thesis:

Publication 1. V M Novotortsev, I S Zakharov, A V Kochura, S F Marenkin, R Laiho, E Lähderanta, A Lashkul, A G Veresov, A V Molchanov, and G S Yur'ev. Ferromagnetism of Manganese-Doped InSb Alloys. *2006 Russian Journal of Inorganic Chemistry* **51** 1627-1631.

Publication 2. A V Kochura, R Laiho, A Lashkul, E Lähderanta, M S Shakhov, I S Zakharov, S F Marenkin, A V Molchanov, S G Mikhailov, and G S Jurev. Synthesis and magnetic properties of Mn-doped $\text{Cd}_{0.1}\text{Zn}_{0.9}\text{GeAs}_2$ solid solutions. 2008. *J. Phys.: Condens. Matter.* 2008. **20** 335220 (5 pp).

Publication 3. I V Fedorchenko, T A Kypriyanova, S F Marenkin, and A V Kochura. Cross-section Si-ZnAs₂ of the Ternary System Zn-Si-As. 2008 *Russian Journal of Inorganic Chemistry* **53** 1139-1143.

Publication 4. Aleksey Kochura, Irina Fedorchenko, Reino Laiho, Alexander Lashkul, Erkki Lähderanta, Sergey Marenkin, and Ivan Zakharov. Growth and magnetic properties of Mn-doped ZnSiAs₂/Si heterostructures. 2009. *Phys.Stat. Sol. (c)* **6** 1336 – 1338.

Publication 5. V M Novotortsev, S F Marenkin, L I Koroleva, T A Kupriyanova, I V Fedorchenko, R Szymczak, L Kilanski, V Domuchowski, and A V Kochura. Magnetic and Electric Properties of Manganese-Doped ZnSiAs₂ 2009. *Russian Journal of Inorganic Chemistry* **54** 1350-1354.

Publication 6. A V Kochura, B A Aronzon, A Lashkul, A A Sidorenko, R De Renzi, S F Marenkin, M Alam, A P Kuzmenko, M S Shakhov, and E Lähderanta. Effect of MnSb clusters on magnetic and electrical properties of (In,Mn)Sb. To be published.

The Author of this dissertation planned the experiments and participated in growing of the crystals and heterostructures, in investigation of structural properties, and in carrying out the measurements of magnetic and transport properties (**publications 1 - 4, 6.**). The Author analyzed

the data, wrote all papers (**publications 1 - 6**) and was the principal author of the **publications 2, 4, 6.**

List of symbols and abbreviations and abbreviations

Symbols

a, b, c	lattice parameters
n	concentration of electrons
B	magnetic field
B_{ext}	external magnetic field
B_a	anisotropy field
B_C	coercive force
C	Curie constant
E_a	activation energy
$f(T), f(r)$	distribution functions of blocking temperatures and cluster size, respectively
g	g-factor
J_{pd}	pd -exchange constant
K	density of the anisotropy energy
k_B	Bolzman constant
M	dc magnetization
M_0	specific magnetization
M_{eff}	magnetization calculated from results of magnetoresistance measurements
M_{FM}	ferromagnetic part of magnetization
M_{PM}	paramagnetic part of magnetization
M_{PM0}	specific magnetization of paramagnetic subsystem
M_s	saturation magnetization of ferromagnetic subsystem
M_{ZFC}	zero-field cooled magnetization
N_{Mn}	manganese concentration
n_{Mn}	concentration of Mn atoms incorporated into lattice
n_{PM}	concentration of superparamagnetic particles
P	spin polarization
p	concentration of holes
p_{eff}	effective number of Bohr magneton
R_0, R_S	normal and anomalous Hall coefficients, respectively
r, d	radius and diameter of clusters, respectively
\bar{r}	most probable radius of clusters
S, s	Mn ions spin and hole spin, respectively
$\langle S_z \rangle$	Brillouin function
T	temperature
T_{AF}, T^*	antiferromagnetic and ferromagnetic coupling parameters, respectively
T_b	blocking temperature
T_C	Curie temperature
T_{C_c}, T_{C_h}	Curie temperate on cooling and on heating, respectively
T_{C_m}	Curie temperate related to the ferromagnetic transition in the InMnSb matrix
T_{eff}	effective temperature
T_m	melting temperature
V	average volume of the particles
V_{int}	spin-independent part of the potential
x	composite of material
α, γ	constants in distribution function of the blocking temperature
β	mass fraction of Mn

δ	mean-square deviation of cluster radius
χ_0	specific susceptibility
χ_{PM}	susceptibility of paramagnetic part
χ_{ZFC}	zero-field cooled susceptibility
η	mass fraction of magnetic precepitate
μ	magnetic moment
μ_{Mn}	magnetic moment per Mn atom
μ_B	Bohr magneton
μ_n, μ_p	electrons and holes mobility, respectively
v	volume of the crystal lattice
u	argument of Brillouin function
θ	diffraction angle
θ_{CW}	Curie – Weiss temperature
λ	wavelength
ρ	resistivity
ρ_H	Hall resistivity
ρ_{OH}, ρ_{AH}	normal and anomalous part of Hall resistivity, respectively
$\frac{\Delta\rho}{\rho}$	magnetoresistance
φ	mass density
ϕ	packing fraction of the powder
σ_s	saturation magnetization

Achronyms

AFM	atomic force microscopy
AHE	anomalous Hall effect
FC	field-cooled
FM	ferromagnetic
MBE	molecular beam epitaxy
OM	optical microscopy
PDA	powder diffraction analyses
PM	paramagnetic
SEM	scanning electron microscopy
ZFC	zero field-coold
XRD	X-ray diffraction

1. Introduction

1.1 Short review and motivation for the research

Today a new branch of electronics, called spintronics, is developing rapidly. In spintronic devices is used materials, which allow to control the spin and charge degrees of freedom [1 - 12]. This is their advantage over traditional electronic devices. One of main difficulties of spin components is the absence of materials, which can operate in temperatures similar to traditional electronics. Using of Fe, Co and Ni is not effective, because of they have different crystal structure and electronic properties with semiconductors. Therefore in the present time the search is carried out in different directions, among which:

1. d-elements doping of materials, which are used in modern electronics (Si, Ge, III-AS and others) [1, 5]. One of most perspective materials for spintronic applications is Mn-doped GaAs [1, 13, 14]. In the past decade many important spintronic applications have been realized based on this material, including electrical-field control of the Curie temperature and magnetization, spin injection into non-magnetic semiconductors, tunneling magnetoresistance and electric current induced magnetization reversal [15 - 19]. However, the highest obtained Curie temperatures for GaMnAs films ($T_C \approx 185$ K) [20 - 22] and for heavily Mn-doped (Ga,Mn)As nanowires ($T_C \approx 200$ K) [23] are lower than the room temperature.

Ternary chalcopyrite semiconductors of the II-IV-As₂ system are considered as structural and electronic counterparts of III-AS compounds [24 - 26]. CdSnAs₂, ZnGeAs₂, CdSnP₂, and ZnGeP₂ are “direct” analogues of the InAs, GaAs, InP, and GaP, respectively. They have better solubility of d-elements and can easily accept a high concentration of Mn atoms, which is a natural property of chalcopyrites used as two-cation semiconductor [27].

Theoretical estimates of magnetic order in Mn-doped II-IV-As₂ compounds showed that only 19 of them can retain ferromagnetic properties and only with higher Mn content [28]. In II-IV-As₂ compounds ferromagnetism above room temperature was experimentally observed first in single-crystal Cd_{1-x}Mn_xGeP₂ films [29]. Now 8 compounds with high temperature ferromagnetic ordering are known among Mn-doped II-IV-As₂ semiconductors (Table 1) [30 - 37]. For such materials the highest $T_C \sim 367$ K has been observed for ZnGeAs₂, doped with Mn [37].

Table 1. Parameters of Mn-doped II-IV-As₂ compounds exhibiting ferromagnetism.

Compound	T_m, K	Crystal symmetry	Unit cell parameters, Å	Enthalpy of formation, kJ/mol	Energy gap, eV	T_c, K (with Mn doping)
ZnGeP ₂	1293	tetragonal, cubic	$a = 5.465;$ $c = 10.711$ $a = 5.433$	-2.17	2.05	318
CdGeP ₂	1072	tetragonal, cubic	$a = 5.741;$ $c = 10.775$ $a = 5.592$	-1.31	1.72	320
ZnSiAs ₂	1369	tetragonal, cubic	$a = 5.611;$ $c = 10.885$ $a = 5.545$	-1.47	1.74	337
ZnGeAs ₂	1148	tetragonal, cubic	$a = 5.672;$ $c = 11.153$ $a = 5.545$	-1.35	1.15	367
CdGeAs ₂	944	tetragonal, cubic orthorhombic	$a = 5.9432;$ $c = 11.2163$ $a = 5.91$ $a = 7.182;$ $b = 7.420;$ $c = 12.761$	-0.84	0.57	355
ZnSnAs ₂	1048	tetragonal, cubic	$a = 5.8466;$ $c = 11.7037$ $a = 5.851$	-1.67	0.65	329
CdSnP ₂	860	tetragonal, orthorhombic	$a = 5.900;$ $c = 11.518$ $a = 12.817;$ $b = 9.826;$ $c = 10.775$	-1.55	1.1	290
ZnSiN ₂	-	orthorhombic	$a = 12.817;$ $b = 9.826;$ $c = 10.775$	-6.8	3.1	280

2. Hybrid structures give number possibilities for spin manipulation. Here ferromagnetic material is inserted to nonmagnetic semiconductor matrix. Incorporating Mn into III-AS compounds layers can substantially alter the observed ferromagnetic characteristics [38 - 41]. The presence of ferromagnetic clusters (MnAs) embedded in the semiconductor matrix (hybrid structures) improves certain device properties of these materials, because of higher ferromagnetic transition temperature T_C [42 - 45]. For example with MnAs inclusions in GaAs matrix T_C exceeds 310 K.

A less studied system is InSb:Mn/MnSb [**publication 1**, 46 - 50]. This class of magnetic materials have some advantage over well-known GaAs:Mn/MnAs structures. Value of $T_c \approx 585$ K [51] for MnSb is much higher than the room temperature. Moreover MnSb has acceptable structural compatibility with traditional electronics materials. These facts stimulates

now interest to growth and investigation of hybrid MnSb/semiconductor (Si, GaAs, GaSb, InP) materials [52 - 57]. Embedding MnSb to semiconductors matrix lead to the magneto-optical effect [54]. InSb is a narrow gap semiconductor (0.18 eV at 300 K) with carrier mobility $\mu_n \approx 8 \text{ m}^2 \cdot \text{V}^{-1} \cdot \text{c}^{-1}$ at 300 K nearly one order more than that of GaAs [58] and with a wide variety of device applications including infrared detectors, imaging systems and high-speed electronic devices [59, 60]. Combining MnSb and InSb properties is capable to produce material for spintronic applications.

It is stimulated interest to elaborate growing process of materials described above and to establish correlation among their structural, magnetic and transport properties.

1.2 Outline of the work

The thesis is devoted to investigation of typical representatives of the Mn-doped II-IV-As₂ semiconductors, including Cd_{1-x}Zn_xGeAs₂:Mn, ZnSiAs₂:Mn bulk crystals, ZnSiAs₂:Mn/Si heterostructures and InSb:Mn alloys belonging to III-As semiconductors, which are structural and electronic counterparts of II-IV-As₂ compounds.

The purposes of the work are the growth of Mn-doped semiconductor compounds with T_C above room temperature to establish the nature of ferromagnetic ordering and to search the influence of the structural peculiarities on magnetic and electrical properties of grown materials.

The thesis contains a summary section and the original papers. The summary section consists of four chapters, characterized below.

Chapter 2 includes mainly growth technology of semiconductors with high T_C and investigation of their structural properties. InSb, Cd_{1-x}Zn_xGeAs₂:Mn and ZnSiAs₂:Mn bulk crystals were grown by direct melting of starting components followed by fast cooling with cooling rate 10 – 12 K/s. Mn-doped ZnSiAs₂/Si heterostructures were grown by vacuum-thermal deposition of ZnAs₂ and Mn layers on Si substrates followed by annealing. The compositional and structural properties of samples were investigated by optical (OM), atomic force (AFM), scanning electron (SEM) microscopy and X-ray powder diffraction analyze (PDA). It is shown that the samples consist of micro- and nano- sizes clusters of an additional ferromagnetic Mn- X phases ($X = \text{Sb or As}$).

Chapter 3 describes magnetic properties of the Mn-doped II-IV-As₂ semiconductors, ZnSiAs₂:Mn/Si heterostructures and InSb:Mn alloys.

Influence of magnetic precipitations on magnetic properties of the investigated materials were examined. It is shown that with relatively high Mn concentration the main contribution to magnetization of samples is by MnSb or MnAs clusters. These clusters are responsible for high temperature behavior of magnetization (i.e. Hopkinsons effect) and relatively high Curie temperature: up to 350 K for Mn-doped II-IV-As₂ and about 600 K for InSb:Mn alloys. The low-field magnetic properties of Mn-doped II-IV-As₂ semiconductors and ZnSiAs₂:Mn/Si heterostructures are connected to the nanosize MnAs particles, having size distribution like Gaussian or several overlapped Gaussians with most probable cluster radius from 3 nm up to 6 nm. Also influence of nanosized MnSb clusters on low-field magnetic properties of InMnSb have been observed. The contribution of paramagnetic phase to magnetization rises at low temperatures or in samples with low Mn concentration. It was found that source of this contribution is not only isolated Mn ions, but also small complexes, mainly dimmers and trimmers formed by Mn ions, substituting cation positions in crystal lattice.

Chapter 4 contains resistivity, magnetoresistance and Hall resistivity (including anomalous Hall effect) measurements in bulk Mn-doped II-IV-As₂ and InSb crystals with their quantitative analysis. The negative magnitoresistance have two sorces: 1) the interaction between delocalized holes *s* and *3d* shells of the Mn ions; 2) giant Zeeman splitting near the cluster interface which is spreads into the paramagnetic matrix resulting in aligning of the carrier spins. At low temperatures in samples with high Mn concentrations low-temperature FM ordering was observed. It is approved by presence of the local maximums on the resistivity vs. temperatures curves in InMnSb samples. Anomalous Hall effect was observed in Mn doped samples and analyzed for InMnSb. It was found that MnX clusters influence significantly on magnetic scattering of carriers.

Chapter 5 is concluding the work, representing summary of the main result.

1.3 Summary of the publications

The thesis is based on the following six articles published in international journals.

Publication 1. V M Novotortsev, I S Zakharov, A V Kochura, S F Marenkin, R Laiho, E Lähderanta, A Lashkul, A G Veresov, A V Molchanov, and G S Yur'ev. Ferromagnetism of Manganese-Doped InSb Alloys. *2006 Russian Journal of Inorganic Chemistry* **51** 1627 - 1631.

Preparation, characterization, electrical and magnetic properties of the InSb:Mn alloys with Curie temperature ≈ 580 K are reported for the first time. Three samples with Mn concentration 0.48; 0.7 and 1.42 wt % were investigated. Presence of micro-size magnetic Mn-Sb (MnSb or Mn₂Sb) inclusions in In_{1-x}Mn_xSb matrix was shown. All samples had *p*-type conductivity with carrier concentration of about $(2 - 4) \cdot 10^{20} \text{ cm}^{-3}$, slightly depending on temperature. Resistivity vs. temperature, magnetoresistance and Hall resistivity vs. magnetic field indicated on existing of low temperatures paramagnetic-ferromagnetic transitions in diluted magnetic semiconductor In_{1-x}Mn_xSb at $T < 7$ K.

Publication 2. A V Kochura, R Laiho, A Lashkul, E Lähderanta, M S Shakhov, I S Zakharov, S F Marenkin, A V Molchanov, S G Mikhailov, and G S Jurev. Synthesis and magnetic properties of Mn-doped Cd_{0.1}Zn_{0.9}GeAs₂ solid solutions. 2008. *J. Phys.: Condens. Matter.* 2008. **20** 335220 (5 pp).

This publication presents the structural, magnetic and transport properties of Mn-doped single crystal Cd_{1-x}Zn_xGeAs₂ ($x = 0.9$). Such compounds were chosen to increase the Mn solubility in CdGeAs₂:Mn above 0.89 wt %. It was found that instead of the usual II-IV-As₂ tetragonal chalcopyrite structure, Cd_{0.1}Zn_{0.9}GeAs₂:Mn crystallized to metastable cubic-like zinc blende structure with lattice parameter practically coinciding with the lattice constant of GaAs. Synchrotron X-ray diffraction measurements reveal persistent MnAs diffraction peaks increased almost proportional to the amount of Mn in the samples. Changing of the lattice parameter when doping with Mn is most probably due to substituting of Mn²⁺ for Cd or Zn in the form of isoelectronic centers. At low concentration Mn started to replace Ge positions in the host lattice. Influence of paramagnetic Mn²⁺ ions on magnetic properties was observed at low temperatures. For the sample with 2.65 wt % Mn a magnetic ordering of matrix was observed by fitting magnetoresistivity vs temperature curves ($T_C < 1.5$ K). It can be described by p-d interaction between charge-carrying holes and localized moments.

Publication 3. I V Fedorchenko, T A Kypriyanova, S F Marenkin, and A V Kochura. Cross-section Si-ZnAs₂ of the Ternary System Zn-Si-As. 2008 *Russian Journal of Inorganic Chemistry* **53** 1139-1143.

To develop a growth method of new high-temperature ferromagnetic structure in this article was constructed a quasi-binary cross-section Si - ZnAs₂ of the Zn - Si - As system. The congruently melting compound ZnSiAs₂ and two eutectics Si + ZnSiAs₂ and ZnSiAs₂ + ZnAs₂ are formed along this cross-section. The component solubilities in ZnSiAs₂ do not exceed 1 mol %. On base of the earlier analysis of the binary subsystems Zn - As, Si - As, and Si - Zn the Zn - Si - As ternary diagram have been analyzed.

Publication 4. Aleksey Kochura, Irina Fedorchenko, Reino Laiho, Alexander Lashkul, Erkki Lähderanta, Sergey Marenkin, and Ivan Zakharov. Growth and magnetic properties of Mn-doped ZnSiAs₂/Si heterostructures. 2009. *phys. stat. sol. (c)* **6** 1336 - 1338.

This paper is based on the report presented in the 16th International Conference on Ternary and Multinary Compounds (Berlin, Germany, 15 - 19 September 2008). Mn-doped ZnSiAs₂/Si heterostructures were grown by vacuum-thermal depositions of ZnAs₂ and Mn layers on Si substrates followed by annealing. Content and structure of the samples were in good agreement with quasi-binary cross-section Si-ZnAs₂ and the Zn - Si - As ternary diagram which was analyzed earlier. Magnetic properties showed existing of two types of magnetic phases: a paramagnetic one with mean magnetic moment $\mu \approx 7.6 \mu_B$, and ferromagnetic one with $T_C \approx 340$ K, formed by MnAs clusters. It is in good agreement with results of magnetic measurements in bulk crystals of Mn-doped II-IV-As₂. The reason of μ exceeding the magnetic moment of Mn²⁺ ion (5 μ_B) when substituting the Zn or Si site is discussed.

Publication 5. V M Novotortsev, S F Marenkin, L I Koroleva, T A Kupriyanova, I V Fedorchenko, R Szymczak, L Kilanski, V Domuchowski, and A V Kochura. Magnetic and Electric Properties of Manganese-Doped ZnSiAs₂ 2009. *Russian Journal of Inorganic Chemistry* **54** 1350-1354.

This publication presents structural, magnetic and transport properties Mn-doped ZnSiAs₂ crystal. X-ray powder diffraction analyses showed that manganese atoms substitute for atoms in the cationic sublattice of ZnSiAs₂. Moreover, by X-ray fluorescence investigation it was found that with increasing manganese percentage, zinc and silicon percentage decreased in proportion.

Samples of ZnSiAs₂:Mn were magnetically sensitive. They were considered as dilute magnetic semiconductors with hole conductivity. The T_C and carrier density increased with increasing manganese content in the samples and reached 337 K. For $T < 50$ K, magnetization increased with decreasing the temperature, pointing out on existing of paramagnetic phase. The ferromagnetic properties of ZnSiAs₂:Mn was defined by MnAs nanoclusters, whose mean radius increased with increasing Mn content (up to 3.6 nm for sample doped with Mn 2 wt %).

Publication 6. A V Kochura, B A Aronzon, A Lashkul, A A Sidorenko, R De Renzi, S F Marenkin, M Alam, A P Kuzmenko, M S Shakhov, and E Lähderanta. Effect of MnSb clusters on magnetic and electrical properties of (In,Mn)Sb. To be published.

Preparation, characterization, electrical and magnetic properties of the InMnSb are reported in this article. Polycrystalline InMnSb samples containing 0.12, 0.5, 0.7 or 1.4 Mn wt % were prepared by solid state reaction with fast cooling rate of 10 - 12 K/s. Samples were large-block InSb polycrystals with microcrystalline MnSb clusters with non-uniform lateral density and mean size from 100 to 600 nm. MnSb clusters have fine structure, they are composed from nanograins with a mean diameter about 24 nm with Gauss-like distribution of the nanograin size. Taking into account the mixture of MnSb clusters, Mn atoms and Mn complexes distributed in InSb matrix the magnetic, electrical and transport properties of the samples were analyzed. A high temperature ferromagnetism in InMnSb is due to MnSb clusters. The paramagnetic background and FM transition in matrix at $T < 10$ K is due to Mn complexes, mainly dimmers, substituting In in the InSb matrix. The Mn solubility in the InSb was estimated to be about 10^{20} cm⁻³. This value is about one order of magnitude more than the solid solubility of Mn in bulk InSb monocrystals. The concentration of Mn complexes is about $3 \cdot 10^{19}$ cm⁻³. However, only small part of Mn ions and complexes located in the In sites contribute to the low temperature FM state.

2. Growth and experimental procedure

2.1 Synthesis of InSb and (Zn,Cd)(Ge,Si)As₂ crystals doped with manganese

Introductory remarks

Indium antimonide doped with manganese was produced by different methods. Single crystal of InMnSb was grown by Chokhralsky method [62 - 64] with manganese concentration N_{Mn} up to $5 \cdot 10^{18} - 1 \cdot 10^{19} \text{ cm}^{-3}$ [63]. Previously this concentration was the limit of solid solubility of Mn in bulk InSb crystals. For practical application, only crystals with $N_{Mn} < 3 \cdot 10^{17} \text{ cm}^{-3}$ were suitable [62]. Growing of InMnSb crystals with Mn doping concentration beyond the equilibrium solubility limit by a horizontal Bridgman technique is reported in [50].

The first attempt to grow InSb films heavily-doped with Mn by MBE was described in [65]. A sequence of Mn-doped InSb films was grown using a substrate temperature of 300 °C or 360 °C. The incorporation of manganese was nearly perfect in wide range of manganese concentrations, and bulk solubility limit (10^{19} cm^{-3}) was reached. There were some signs that a metastable solid solution was obtained or possibly an Mn-rich phase was precipitated in the bulk of the films [65].

Low-temperature MBE with substrate temperature about 170 °C were used to avoid forming of precipitation phases and to rise manganese solubility in InSb [66-68]. This way was grown ferromagnetic In_{1-x}Mn_xSb films with T_C reaching 8.5 K ($x = 0.028$) [66, 67] and 20 K ($x = 0.1$) [68].

The value of $T_C \approx 130$ K was obtained in bulk InMnSb synthesized by controlled ambient annealing technique [69]. T_C above room temperature was observed in InMnSb films grown by pulsed laser deposition [70] and liquid phase epitaxy [49].

Recently a high temperature FM ($T_C = 590$ K) was reported in In_{1-x}Mn_xSb with $x \leq 0.035$ grown by metalorganic vapor phase epitaxy [71]. Spin-dependent magnetotransport at room temperature (with spin polarization $P \approx 50\%$) was observed in a p-InMnSb/n-InSb magnetic semiconductor heterojunction grown in the same way [72].

InSb:Mn

Direct melting of indium antimonide with manganese and antimony was used to synthesize polycrystalline InMnSb samples [**publication 1**]. The starting materials were single crystal n-type InSb ($n = 3 \cdot 10^{15} \text{ cm}^{-3}$, $\mu_n > 4 \cdot 10^5 \text{ cm}^2/(\text{V} \cdot \text{s})$ at $T = 77$ K), high purity antimony (5N) and bisublimed manganese (4N). The components were prepared as powder with average particle sizes of 5 – 10 μm. The starting mixtures were weighed on a torsion balance with an accuracy of $\pm 1 \cdot 10^{-6}$ g. The samples were synthesized in evacuated (10^{-2} Pa) quartz ampules, etched in mixtures of analytical-grade HF, HCl, and HNO₃, washed with deionized water, held at 400 K in

a drying oven and coated with pyrolytic graphite. Ampules were placed in the tube furnace in position with isothermal conditions throughout the length of the ampule. The synthesis was performed at temperature 1050 K during 24 h. This temperature exceed the InSb melting temperature (800 K) to make conditions for better homogenization of the melt. To reach the maximal solubility of manganese in InSb the final step of growing procedure was fast cooling (cooling rate 10 -12 K/s) of ampules. This non equilibrium growth method was chose to exceed the solubility limit of Mn in bulk InSb $5 \cdot 10^{18}$ - $1 \cdot 10^{19}$ cm⁻³ at equilibrium growth [63]. Prepared samples contained 0.12; 0.47; 0.7 and 1.42 mas.% of Mn and labeled as #A1, #A2, #A3 and #A4, respectively.

(Zn,Cd)GeAs₂:Mn

The most probable quasi-binary sections in which $A^{II}B^{IV}C^V_2$ compounds can form are the $A^{II} - B^{IV}C^V_2$, $A^{II}_3C^V_2 - B^{IV}C^V$, and $B^{IV} - A^{II}C^V_2$ sections (Fig. 1). The most optimal way to synthesize ternary compound is through the interaction of the components along the $B^{IV} - A^{II}C^V_2$ section. The preparation of the batch along this section considerably decreases the free volume in synthetic ampules as compared with the batch consisting of individual components. This ensure the preparation of the stoichiometric composition of the synthesized ternary compound. The

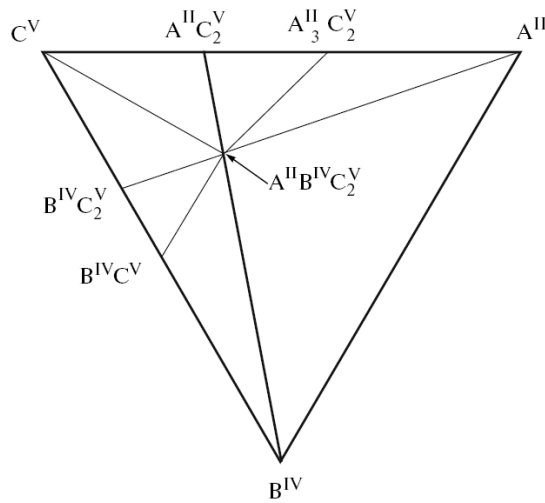


Fig.1. Triangulation of the $A^{II}B^{IV}C^V_2$ system.

preparation of a batch along the $A^{II} - B^{IV}C^V_2$ and $A^{II}_3C^V_2 - B^{IV}C^V$ sections is less efficient since the $B^{IV}C^V_2$, $A^{II}_3C^V_2$, and $B^{IV}C^V$ compounds are more difficult to synthesize than the $A^{II}C^V_2$ compounds.

To grow of $(Zn,Cd)GeAs_2$ samples, as starting materials was used monocrystalline cadmium and zinc diarsenides prepared by vertical Bridgman technique, high-purity germanium

(5N) and manganese (3N) [publication 2]. The amounts of the starting materials were controlled by weighing with accuracy of 0.005%. Because zinc and cadmium diarsenides dissociate upon heating with arsenic vapour evolution, small value of arsenic was added to bathes to adjust stoichiometry. The weight of this additional arsenic was calculated from the arsenic partial vapour pressure of ZnAs_2 and CdAs_2 and the volume of the ampoule in which the synthesis was carried out. The components were prepared as powders with average particle sizes of 5 – 10 μm . Total mass of batches placed into quartz ampoules was 9 – 10 g. The ampoules were evacuated to $1 \cdot 10^{-2} \text{ Pa}$ and sealed. The synthesis temperature was 1175 K (close to $T_m = 1148 \text{ K}$ of ZnGeAs_2) and the synthesis duration was 36 h. To provide maximal solubility of manganese the cooling rate was 10 – 12 K/s (Fig.2a). Prepared samples of $\text{Zn}_{0.9}\text{Cd}_{0.1}\text{GeAs}_2$ contained 0; 1.13; and 2.65 mas.% of Mn and labeled as #B1, #B2, and #B3, respectively.

The procedure to prepare of Mn-doped CdGeAs_2 was like described above for the $\text{Zn}_{0.9}\text{Cd}_{0.1}\text{GeAs}_2\text{:Mn}$. The synthesis temperature was 950 K (close to $T_m = 940 \text{ K}$ of CdGeAs_2). Prepared samples of CdGeAs_2 contained 0.25; 1; and 6 wt% of Mn and labeled as #C1, #C2 and #C3, respectively.

CdGeAs_2 single crystals doped with Mn were grown by a vertical Bridgman method.

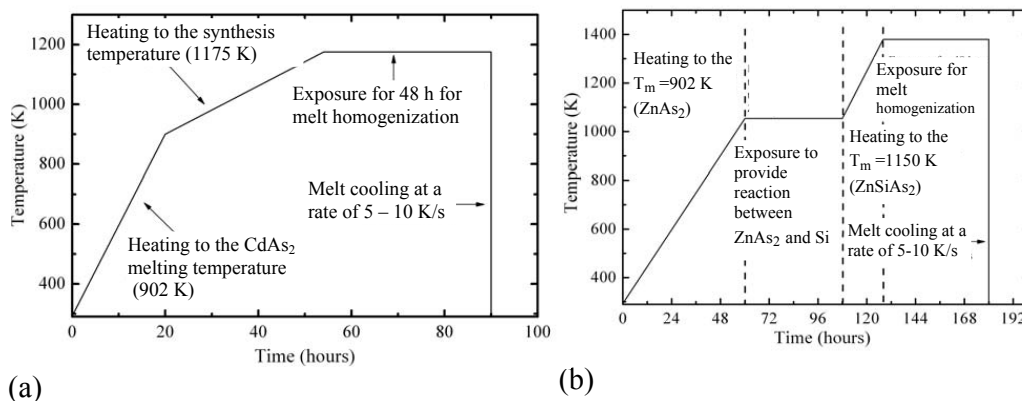


Fig.2. Temperature during the synthesis of manganese-doped $\text{Zn}_{0.9}\text{Cd}_{0.1}\text{GeAs}_2$ (a) and ZnSiAs_2 (b).

Original materials for crystal growth were synthesized from appropriate amounts of ground CdAs_2 and Ge crystals (7N) and Mn metal (4N). The process was done under a vacuum of 10^{-2} Pa in graphitized ampoules with a capillary tip, which contained a single crystal CdGeAs_2 seed. The temperature of melting zone was 962 K. To homogenize the melt, the ampule was rotated at 3 rpm. After this step, the ampule was lowered in a steel container to the low-temperature zone (773 K) at a rate of 0.05 cm/h. The resulting single crystals measured 16 –

18 mm in diameter and up to 120 mm in length. Two single crystals of CdGeAs₂ contained 0.006 and 0.89 wt % of Mn and labeled as #D1 and #D2, respectively.

ZnSiAs₂:Mn

Specimens with various Mn concentrations were synthesized by direct melting of high-purity Si, ZnAs₂ and Mn powders at a temperature of 10 to 15 K above the ZnSiAs₂ melting point (1369 K). The reaction ZnAs₂ + Si = ZnSiAs₂ versus time mode is shown in Fig.2b. This method was developed by analyzing the Zn-Si-As ternary system and its quasibinary sections (Fig. 3).

The synthesis of ZnSiAs₂ by SiAs₂ – Zn section was complicated by high temperature and peritectic nature of SiAs₂ melting. If one uses the direct melting of Zn, Si, and As in synthesis, it is difficult to retain stoichiometry because of highly volatile arsenic. The synthesis by ZnAs₂ – Si section is most suitable because of congruent ZnAs₂ melting and low pressure of As vapor (Table. 2).

Table. 2. Synthesis conditions of ZnSiAs₂.

Section	Melting mode	Achieving of stoichiometric composition	Homogenizing annealing
Si+Zn+2As	<i>As vapor pressure is high</i>	<i>difficult</i>	<i>difficult</i>
Zn+SiAs ₂	<i>incongruently</i>	<i>difficult</i>	<i>difficult</i>
Si+ZnAs ₂	<i>congruently</i>	<i>easy</i>	<i>easy</i>

Three polycrystalline ZnSiAs₂ samples doped with 0, 1 and 2 wt % Mn, labeled as #E1, #E2 and #E3, respectively, were produced [publication 5].

Ferromagnetic Si/ZnSiAs₂:Mn heterostructures were synthesized by a liquid-phase epitaxy of the Mn-doped ZnAs₂ melt-solution with ZnSiAs₂ on monocrystal Si substrates (Fig. 4) [publication 4]. First a vacuum-thermal method was used to deposit ZnAs₂ and Mn films with a thickness ratio 10:1 on oriented Si (001) substrates. Further the solution-melt was produced by an annealing with time period 48 h at temperatures of 1173 K or 1273 K in Zn and As vapors. During thermal treatment ZnAs₂ and Si substrates were in interaction with the melt of Mn-doped solution. During cooling the samples of ZnSiAs₂ was formed by the reaction ZnAs₂ + Si = ZnSiAs₂ in accordance with liquidus line on cross-section of Si – ZnAs₂ of the system Zn-Si-As [publication 3].

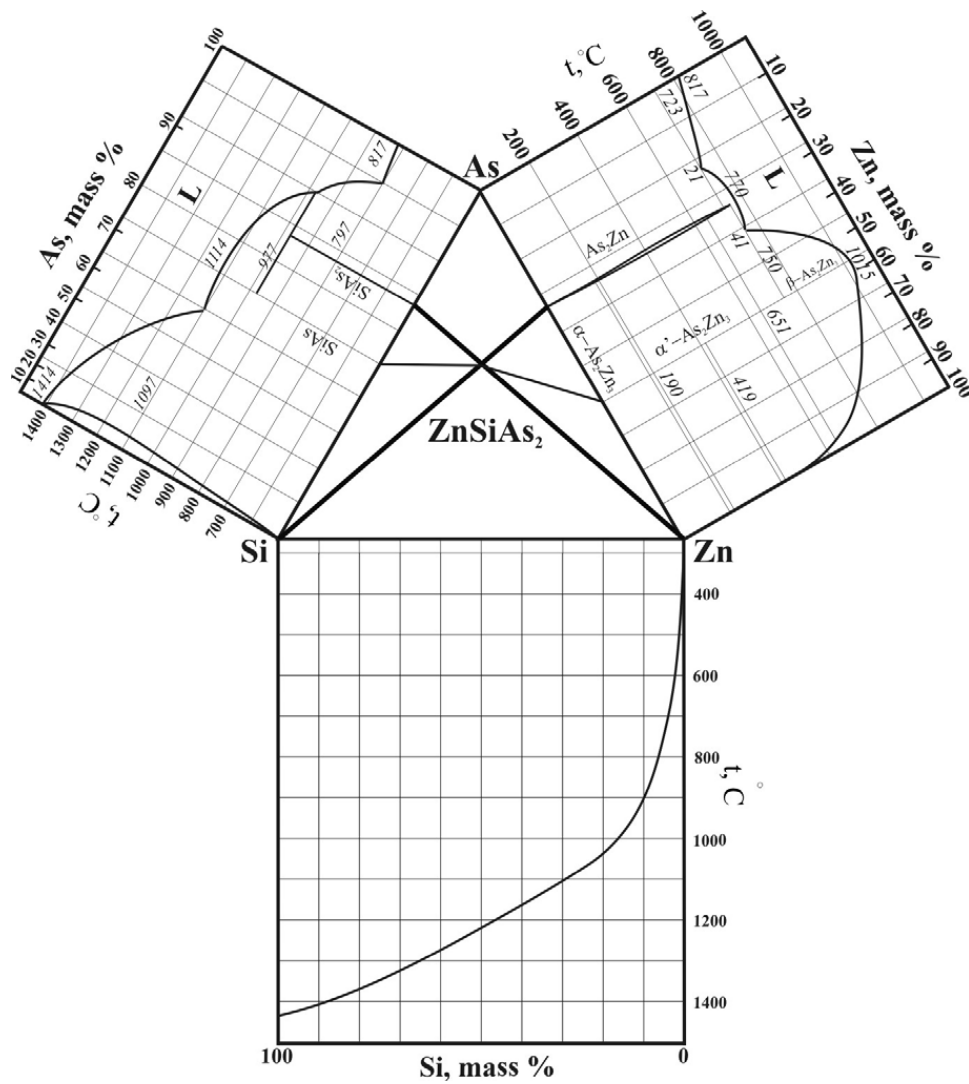


Fig. 3. Phase diagram triangulation of Zn-Si-As system. [publication 3].

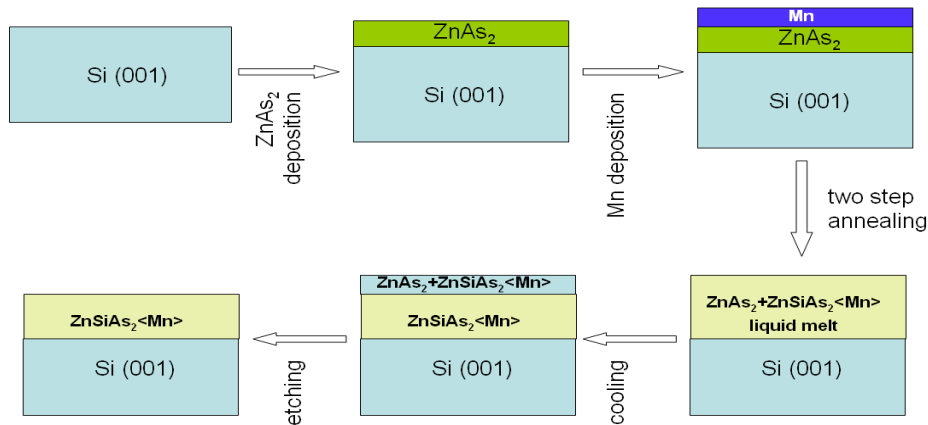


Fig. 4. Synthesis scheme of manganese-alloyed ZnSiAs₂/Si heterostructure.

Heterostructure ZnSiAs₂/Si Sample doped with Mn annealing at 1173 K was synthesized. This was labeled as #F1

2.2 Structural properties of the grown samples

2.2.1. OM, ESM and AFM examination of the structure

Samples for structural investigation were cut from bulk by wire saw (*Model 850*, South Bay Technology, Inc.) and polished chemically-mechanically by *Metaserv 3000* grinder-polisher (Buehler LTD) with SiO₂ colloidal suspension (20 nm) on final stage.

OM images of sample surface were taken by structural analyzer “Epiquant” with magnification up to 1000×.

Scanning electron microscope *Quanta 600 FEG* (FEI Company) equipped with analytical systems (energy dispersive spectrometer, wavelength dispersive X-ray spectroscopy and electron backscatter diffraction) was used to obtain surface images and to determine elemental composition of samples.

Samples structure was investigate by *SmartSPM 1000* (AIST-NT Co) scanning probe microscope in AFM mode.

OM image, AFM and SEM investigations showed that the samples grown under non equilibrium conditions contained clusters which correspond to the three-dimensional microcrystalline MnSb or MnAs inclusions (Fig. 5a) and have granular structure (Fig. 5b,c,d).

Fig. 5a shows InMnSb polycrystalline sample with microcrystalline clusters seen as black points. The lateral density of clusters is not uniform and there are regions with very small concentration.

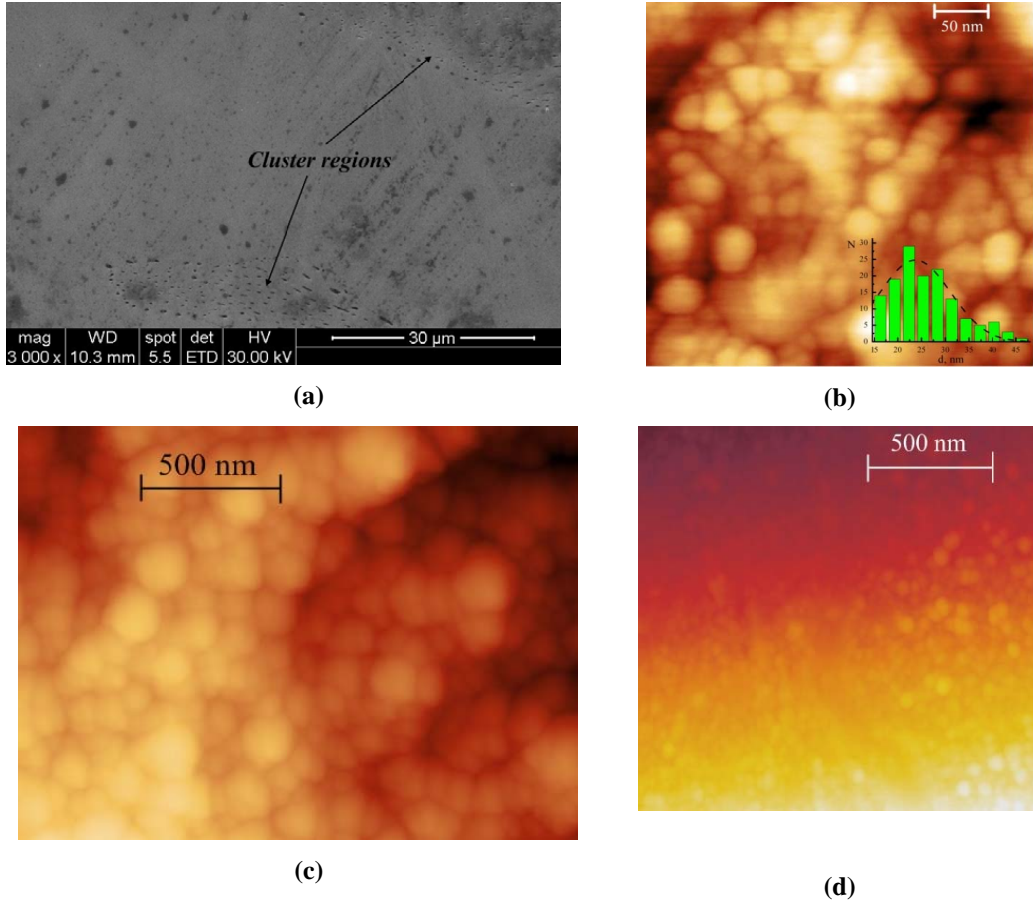


Fig. 5. SEM (a) and AFM (b) images of InMnSb sample #A4 [publication 6], and AFM images of Mn-doped CdGeAs₂ samples #C1 (c) and #C3 (d). Clusters and granular structure of samples is clearly visible.

The lateral size of these clusters ranges mainly from 100 to 600 nm. The structure of one of these clusters is presented in the Fig. 5b showing that sample #A4 has fine structure and is composed from nanograins with a mean size about 24 nm and Gauss-like distribution of the nanograin diameter. Similar structure of InMnSb alloys was also observed and described in Ref. 73.

A granular structure was observed also in II-IV-As₂:Mn compounds (Fig. 5c and d). The mainly part of grains have size from 10 nm up to 150 nm.

Energy dispersive analyze showed that the clusters in InMnSb and II-IV-As₂:Mn samples are formed by Mn-Sb (MnSb or Mn₂Sb) and Mn-As phases, respectively. Additional phases were not detected accurately because of two reasons. The first is small size of clusters. The

electron beam penetration exceeds the mean diameter of a cluster. Therefore the peaks of matrix atoms were observed on dispersive curves together with cluster atoms, and quantitative analysis of cluster composition is not possible. Second, for MnSb, there is a problem of nonstoichiometry, which comes from the phase stability of the NiAs structure in the binary phase diagram of the Mn-Sb system [51]. For example Mn content x in the $Mn_{1+x}Sb$ compounds can change from 0 up to 0.28 [74].

Examples of OM and SEM images of Mn-doped $ZnSiAs_2/Si$ heterostructure are presented in Fig. 6 .

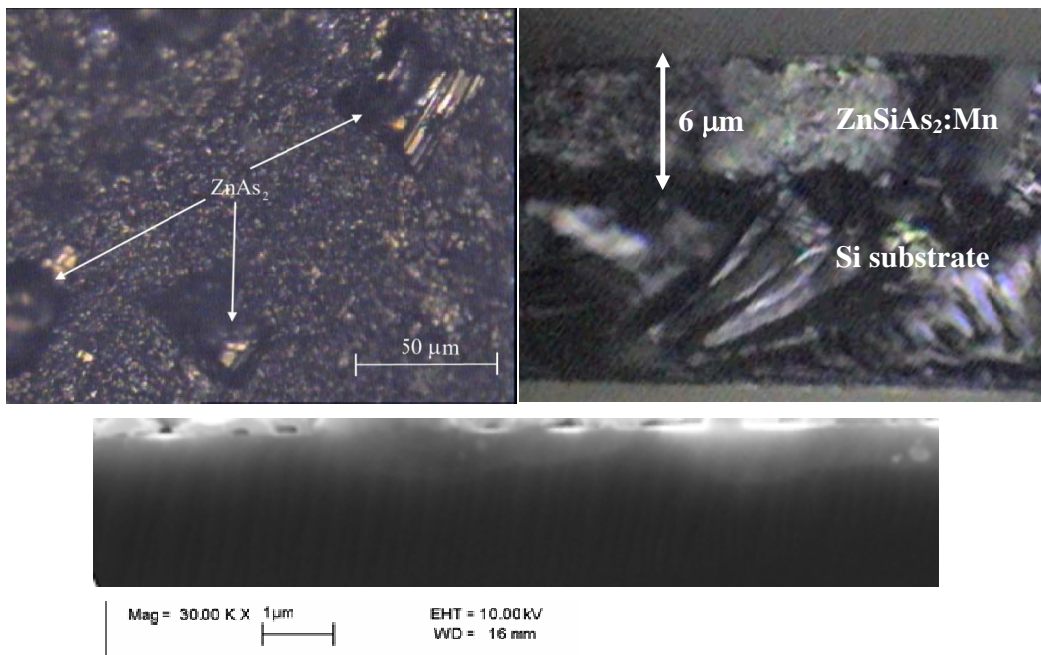


Fig.6. OM images of the bulk surface of the as-grown layer (a) and the chip (b) of the Mn-doped Si/ $ZnSiAs_2$ heterostructure and SEM image (c).

It was observed that the surface contains micro-crystals (Fig. 6a) with a composition close to $ZnAs_2$ (Zn content about 31, As content about 69 wt %, mass fraction of Si below 1%). The surface had small compound of $ZnSiAs_2 - Si - SiAs$ eutectic. These micro-crystals were removed by etching. The contents of Zn, Si, and As on the surface of the etched heterostructure were 28, 12, and 60 wt %, respectively, closely related to the composition stoichiometry [publication 4]. The $ZnSiAs_2$ -Si interface (Fig. 6b) was sharp. It is typical for reaction diffusion and indicates low solubility of the components in the $ZnSiAs_2$. Fig 6c demonstrates high

homogeneity of the ZnSiAs₂ layer. Some inclusions are observed only on 0.2 – 0.3 μm depth from the surface.

2.2.2 X-ray powder diffraction analyses

X-ray powder diffraction (XRD) experiments were carried out using the DRON-2 X-ray diffractometer (CuK_α radiation, $\lambda = 1.5405 \text{ \AA}$, $\theta = 0^\circ - 100^\circ$) and the synchrotron radiation from the second channel of a VEPP – 3 electron/positron accelerator at the Institute for Nuclear Physics (Novosibirsk, Russia). Diffraction patterns were recorded three times on a high-resolution diffractometer in $\Delta 2\theta = 0.005^\circ$ steps with the incident and diffracted beams monochromatized. After each accelerator start, the radiation wavelength $\lambda = 1.3828(1) \text{ \AA}$ was adjusted to the reflection from the (400) plane of a silicon single crystal. The ICSD database was used to analyze diffraction patterns.

The compound ZnGeAs₂, which exist along the ZnAs₂ – Ge section, has a cubic – chalcopyrite phase transition at 1128 K [75]. The cubic (sphalerite-type) ZnGeAs₂ phase has lattice parameter $a = 5.644 \text{ \AA}$ [76]. Analyses of synchrotron radiation diffraction patterns (Fig. 7) showed that all Zn_{0.9}Cd_{0.1}GeAs₂:Mn samples (#B1 - #B3) crystallized in sphalerite space group $F4/3m$, because the high cooling rate froze the metastable cubic structure of ZnGeAs₂. The unit cell parameter for Zn_{0.9}Cd_{0.1}GeAs₂:Mn was greater than for Zn_{0.9}Cd_{0.1}GeAs₂. This is understandable because the Cd – As bond length (2.629 Å) is longer than Zn – As bond length (2.455 Å), and the unit cell parameter should increase in response to a partial substitution of cadmium ions for zinc ions. The unit cell of the solid solution slightly increased with increasing manganese level (sample #B1, $a = 5.647 \text{ \AA}$, sample #B2, $a = 5.648 \text{ \AA}$; sample #B3, $a = 5.651 \text{ \AA}$); this small increase is explained by the generation of substitutional solutions in the cation sublattice of ZnGeAs₂. Mn atoms form isoelectronic centers (Mn²⁺) placing on Cd or Zn sites. In forfold coordination the effective radius of Mn²⁺ is 0.66 Å and the radii of Zn²⁺ and Cd²⁺ are 0.6 and 0.78 Å, respectively, while the radius of Ge⁴⁺ is 0.39 Å [77]. As the lattice parameters of the undoped sample #B1 and sample #B2 with the smallest Mn concentration were almost similar, it is likely that Mn at small concentrations replaces mostly Zn²⁺ or Cd²⁺. When Mn content is higher Mn²⁺ ions start to replace Ge⁴⁺.

Traces of MnAs phase were revealed by analysis of XRD patterns. The intensity of MnAs reflections increased almost in proportion with increasing manganese level. The inset in Fig 7 shows that the diffraction pattern for sample #B3 shows considerable number of the theoretically calculated MnAs diffraction peaks.

The XRD patterns of InMnSb samples had only strong InSb peaks. The lattice constant a changed from 6.4794 Å (sample #A1) to 6.4779 Å (sample #A4). Atomic radii of Mn and In are

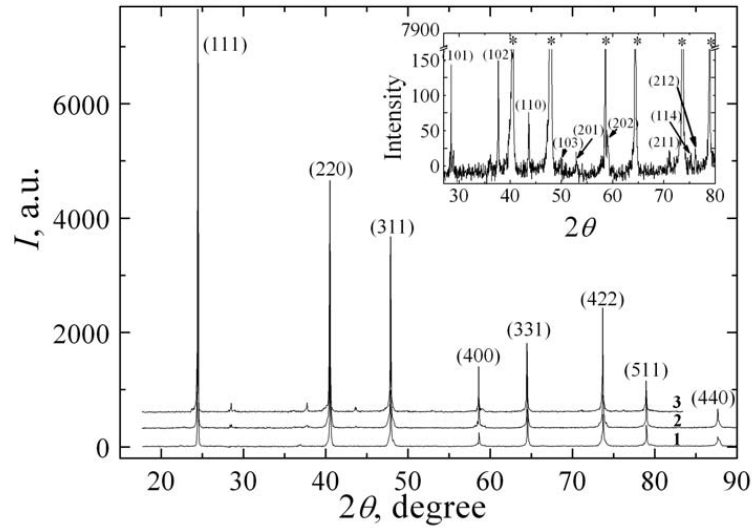


Fig. 7. Synchrotron X-ray diffraction patterns of $Zn_{0.9}Cd_{0.1}GeAs_2$ with Mn. Inset: enlarged part of the diffraction pattern of sample #B4 with Miller indexes shown for MnAs ($P6_3/mmc$: $a = 4.139$ Å, $c = 5.753$ Å) and diffraction peaks of $Zn_{0.9}Cd_{0.1}GeAs_2$, labeled by stars [publication 2].

1.27 and 1.67 Å, respectively [77]. So the decrease of a can be explained by formation of $In_{1-x}Mn_xSb$ solid solution when Mn atoms substitute In sites. This is in agreement with the p -type conductivity of all samples because Mn acts as an acceptor when in In position. Small traces of the second phases (four small peaks), probably Mn-Sb compounds were observed only with help of synchrotron radiation [publication 1].

All $CdGeAs_2:Mn$ and $ZnSiAs_2:Mn$ samples had chalcopyrite-type structure (space group $I4/2d$). The lattice parameters of single crystal samples #D1 and #D2 were $a = 5.944$ Å, $c = 11.211$ Å and $a = 5.940$ Å, $c = 11.200$ Å, respectively. Change of the lattice parameters can be interpreted as evidence that Mn substitutes for Cd sites and can occupy vacant As sites. For polycrystalline $CdGeAs_2:Mn$ samples was observed that the crystal lattice parameters changed nonlinearly with increasing Mn concentration, not complying with the Vegard's law [79]. When the Mn concentration increased to 1 wt % the parameter a decreased from 5.965 Å (sample #C1) to 5.952 Å (sample #C2). For sample #C3 (6 wt% Mn) $a = 5.958$ Å. It is in agreement with $Zn_{0.9}Cd_{0.1}GeAs_2:Mn$ samples when Mn at small concentrations replaces mostly A^{II} positions and with increasing Mn content start to occupy the B^{IV} positions in $A^{II}B^{IV}C^V_2$ compounds.

Table 3 [publication 5] display the lattice parameters of ZnSiAs₂:Mn samples. The parameter *a* increased with increasing manganese content, whereas the parameter *c* remained almost invariable. This means that Mn atoms substitute positions in the cation sublattice of ZnSiAs₂. Zn – As (2.469 Å) and Si – As (2.345 Å) bond lengths are short in comparison to Mn – As (2.579 Å) bond length. Therefore the variation in unit cell parameters in ZnSiAs₂:Mn indicates the formation of solid solutions via the substitution of Mn for Zn and Si atoms. XRD results were in agreement with X-ray fluorescence data. Distributions of all components in ZnSiAs₂:Mn samples were uniform and the ratio of their concentration corresponded to the ZnSiAs₂ stoichiometry. Moreover, with increasing Mn percentage, Zn and Si percentages decreased in proportion [publication 5].

Table.3 Lattice parameters of ZnSiAs₂:Mn as a function of manganese content.

Mn, wt %	<i>a</i> ±0.001, Å	<i>c</i> ±0.001, Å
0	5.6087	10.8783
1	5.6129	10.88008
2	5.6151	10.8812

The difference between unit cell parameters of ZnSiAs₂ (5.6087 Å) and Si (5.431 Å) is 3.2 % and for [001] orientation is less than 2% (Fig. 8). This difference slightly increase with increasing Mn content. Anyhow the ZnSiAs₂:Mn is a suitable material for the silicon technology. Note that the structural compatibility Zn_{0.9}Cd_{0.1}GeAs₂:Mn and GaAs (5.653 Å) is better than ZnSiAs₂ and Si. The lattice parameters Zn_{0.9}Cd_{0.1}GeAs₂:Mn differ from that of GaAs less than 0.04 % (Fig 8).

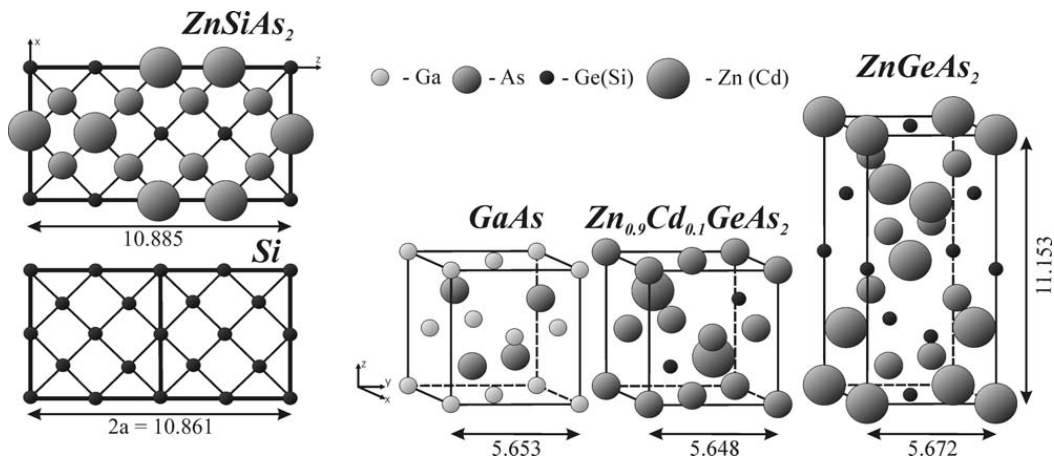


Fig.8. Examples of compatible crystal structures of traditional electronic engineering materials: Si, GaAs and II-IV-As₂ compounds [publications 2 and 5].

3 Magnetic properties of InSb and II-IV-As₂ semiconductors doped with Mn

3.1 Experimental procedure

The dc magnetization, M , was investigated with a superconducting quantum interference device (SQUID) magnetometer (model S600, Cryogenics ltd.). The measurements were performed separately between 3 – 310 K and 260 K – 580 K in fields up to $B = 6$ T. Before every measurement the sample was annealed for 0.5 – 1 h at 420 K for ternary II-IV-II₂ compounds and 600 K for III-V compounds to remove possible remanent magnetizations. Annealing temperatures were chosen to be above the maximal T_C for II-IV-As₂:Mn (367 K) or T_C for MnSb (585 K). The dependence of $M(T)$ was measured in B between 5 G and 500 G after cooling the sample from 300 K to 3 – 5 K in zero field ($B < 0.1$ G) or in the field of the measurements, yielding the data in the zero-field cooled (M_{ZFC}) and the field-cooled (M_{FC}) regimes, respectively. To reach magnetic saturation the dependence $M(T)$ was measured at $B = 50$ kG. Magnetization vs. magnetic field curves ($M(B)$) were investigated in two regimes: 1. **a low-field regime** with B between 0 G and 100 G used for the correct estimation of the coercive force; and 2. **a normal-field regime** with B between 70 G and 60 kG.

The samples for magnetization experiments were cut from bulk crystals. Before measuring the samples were cleaned in boiling chemically pure methanol.

Our SQUID magnetometer is able to measure magnetic moment up to $2.5 \cdot 10^{-5}$ A·m². Therefore the mass of samples must be chosen so that the magnetic signal will not reach the upper limit and the mean sample mass was about 10 mg. Samples were weighed on a torsion balance with an accuracy of $\pm 1 \cdot 10^{-6}$ g. The shape of samples was close to thin plate (two dimensions were much larger than the third one) so demagnetizing factor was about 1 in parallel field direction.

Control of the sample temperature was done with flowing helium gas with an accuracy of 0.2 %, as measured using a carbon-glass thermometer.

3.2. Influence of magnetic precipitations on magnetic properties of investigated materials

3.2.1 MnAs precipitates in II-IV-As₂:Mn

Typical temperature dependences of the magnetizations for Mn-doped II-IV-As₂ compounds are shown in Fig. 9a. The $M(T)$ dependence for samples is complicated. At $T > 100 - 150$ K the $M(T)$ shape is characteristic of the ferromagnet. At low temperatures is seen a sharp increase of magnetization with decrease of temperature. This can be interpreted as an additional contribution of a paramagnetic phase.

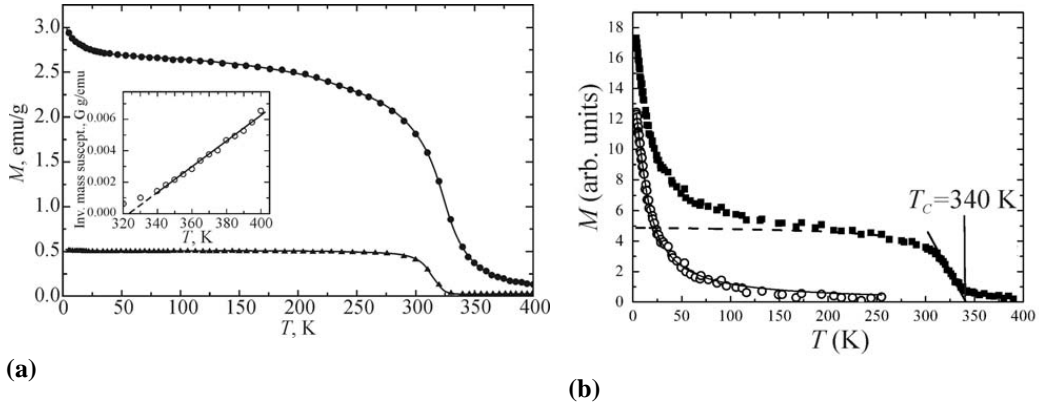


Fig. 9. Temperature dependence of the magnetization: (a) for sample #B2 measured at $B = 500$ G (triangles) and $B = 50$ kG (circles). Inset: temperature dependence of the inverse susceptibility above T_C [publication 2]. (b) for Mn-doped Si/ZnSiAs₂ heterostructure #F1 measured at $B = 50$ kG (squares). The paramagnetic part of the magnetization is shown by the circles with the solid curve calculated as the “best” fit of the Langeven function (see Eq. 2 below). The dashed line is magnetization of the FM phase [publication 4].

The FM part of magnetic multi-phase sample defines the Curie temperature. To determinate the T_C by the fitting the Brillouin function with standard Belov – Arrott method is incorrect; because we examined magnetically heterogeneous samples. In this case the value of T_C

Table 4. Curie temperatures of ferromagnetic Mn-doped II-IV-As₂.

Compound	Sample number	T_C , K
Zn _{0.9} Cd _{0.1} GeAs ₂	#B2	349
	#B3	351
CdGeAs ₂	#C3	337
ZnSiAs ₂	#E1	325
	#E2	337
ZnSiAs ₂ /Si	#F1	340

must be estimated by extrapolation of the steepest part of the $M(T)$ curve to the intersect of T -axis. T_C determined in this way are shown in the Table 4 for Mn-doped ternary compounds at $B = 50$ kG (data taken from publications 2, 4, 5). For the sample #B3 the T_C is 327 K and 323 K in magnetic fields $B = 500$ G and $B \approx 0$ G, respectively. An extrapolation of the linear high-temperature part of the inverse susceptibility at $B = 50$ kG gives the PM Curie temperature 324 ± 6 K for sample #B2 (Inset of Fig. 9a) and 327 K for sample #B3 [publication 2]. The situations

when T_C was decreasing up to 320 – 330 K with magnetic field decreasing and PM T_C belonged to the same interval were observed for all other Mn-doped II-IV-As₂ samples, exhibiting ferromagnetism.

These results, together with synchrotron X-ray PDA, give strong evidence that high-temperature ferromagnetism in our samples originates from MnAs phase.

MnAs is ferromagnetic semimetal. In zero magnetic field at $T < 306$ K and $T > 394$ K the MnAs has hexagonal structure and at $306 < T < 394$ K has orthorhombic structure ($Pnma$) [80]. One magnetic peculiarity of this material is that T_C depends not only on the value of the magnetic field, but also on the measurement mode. In zero field $T_{Cc} = 306$ K on cooling and $T_{Ch} = 317$ K on heating. When B is increased from 0 to 60 kG the values of T_{Cc} and T_{Ch} are shifted to higher temperatures by about 20 K and 30 K, respectively. The second peculiarities of MnAs is magnetic phase transition near 394 K when lattice structure changed on heating from orthorhombic PM phase with the magnetic moment per Mn atom $\mu_{Mn} \approx 2 \mu_B$ (μ_B is Bohr magneton) to hexagonal PM phase with $\mu_{Mn} \approx 3.4 \mu_B$ [80]. These features allow to determine the MnAs phase by magnetic measurements. This is seen in Fig.10 for single crystal $\text{Cd}_{0.964}\text{Zn}_{0.036}\text{GeAs}_2$ doped with Mn (2.18 wt%), grown at the equilibrium conditions¹.

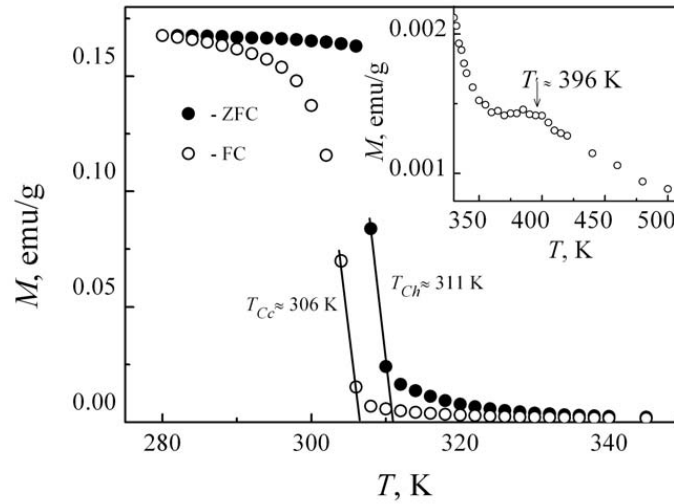


Fig.10. Identification of the ferromagnetic MnAs phase of single crystal $\text{Cd}_{0.964}\text{Zn}_{0.036}\text{GeAs}_2\text{:Mn}$ based on the Curie temperature measurements in ZFC and FC magnetizations ($B = 500$ G). Inset: the high-temperature $M(T)$ part indicating the phase transition between paramagnetic orthorhombic and hexagonal crystal structures of MnAs.

¹ This sample was synthesized by Dr. Mikhailov S.G. and used only for magnetization measurements.

In our Mn-doped II-IV-As₂ crystals the difference between M_{ZFC} and M_{FC} near the Curie temperature was displayed even in strong magnetic field (50 kG), but the high temperature magnetic phase transition (near 394 K) was not clearly observed.

The mass fraction of MnAs was $\eta = 0.0186$ and 0.0479 , and that of Mn was $\beta = 0.0036$ and 0.0063 in the samples #B2 and #B3, respectively. This was estimated from the difference between the saturation magnetization of MnAs, $\sigma_s \approx 123$ emu/g (260 K) [81], and the magnetization of Zn_{0.9}Cd_{0.1}GeAs₂ samples at $T = 260$ K and $B = 50$ kG. Moreover, the small difference between the lattice parameters of these samples indicates that β has to be small and main part of Mn atoms are in MnAs phase.

3.2.2 MnSb precipitates in InMnSb

All InMnSb samples were high-temperature ferromagnetic. As shown in Fig. 11a, a rapid increase in the $M(T)$ curves is observed below 20 K. The decrease of the magnetization is slow between 20 K – 500 K, but it is more rapid again above $T \approx 500$ K. In addition, this high temperature $M(T)$ dependence look like a traditional Brillouin-like $M(T)$ curve in FM, indicating presence of a magnetic transition. For experimental reasons the temperature of our measurements was limited to 580 K but, as can be estimated from Fig. 11a, in all samples T_C is slightly above 600 K at 50 kG. This value is very close to T_C of the MnSb phase (585 K), the presence of which was revealed in our samples by the structural and X-ray PRD analyses.

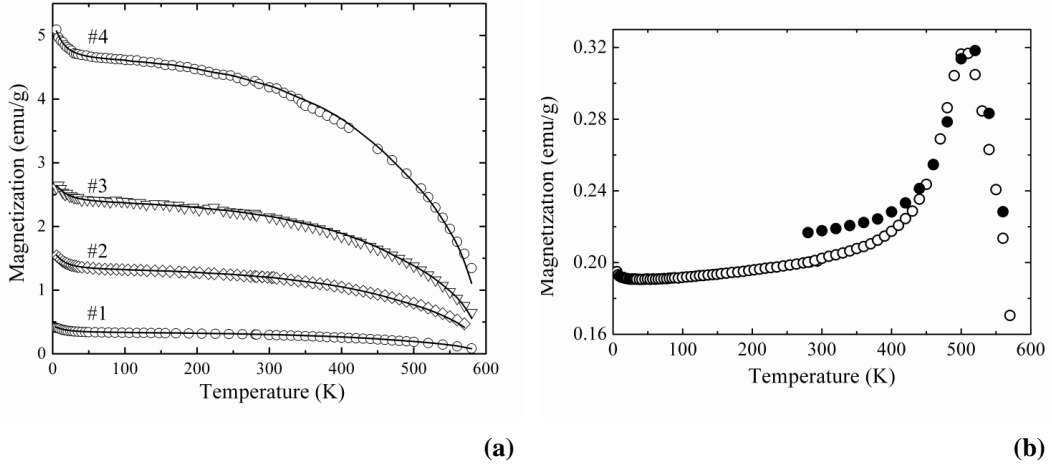


Fig. 11. Temperature dependence of the magnetization of InMnSb samples #A1 - #A4 measured in strong magnetic field (a) and sample #A4 in weak magnetic field (b) (the solid and open circles present M_{FC} and M_{ZFC} , respectively) [publication 6].

Earlier were observed the deviations between the values of T_C in MnSb crystals [82]. It was explained by variations of the Mn content in MnSb where excess Mn atoms have their spins directed antiparallel to the spins of the normally located Mn atoms. This leads to decreasing of T_C and the effective number of μ_B per Mn ion. When the content of excess Mn atoms is less than 50%, T_C is close to that of MnSb. Moreover the maximal solubility of Sb in MnSb corresponds to stoichiometric composition [74]. Therefore MnSb clusters in our InMnSb samples have the composition close to stoichiometric.

The $M(T)$ curves measured in ZFC and FC regime are shown in Fig.11b. After reaching the maximum just below T_C (about 510 K) $M(T)$ decreases sharply when the temperature is increased. This behavior is similar to the Hopkinson effect observed in a bulk MnSb crystals [83] with big non-interacting single-domain particles [84]. Origin of this effect is competition between temperature dependencies of a saturation magnetization and of an anisotropy field. According to the theory, the magnetization of a randomly oriented system in a small field is [85]

$$M(T) = \frac{2}{3} \phi \frac{\sigma_s(T)}{B_a(T)} B, \quad (1)$$

where $\sigma_s(T)$ is the bulk saturation magnetization and $B_a(T)$ is the anisotropy field of the particles ϕ is the packing fraction of the powder. $B_a(T)$ decreases much faster than $\sigma_s(T)$ in a small field when increasing the temperature. Because of this competitive effect there is an overall increase in magnetization which reaches a maximum just below T_C .

3.3 Magnetism of diluted magnetic semiconductor matrix

II-IV-As₂

Samples of II-IV-As₂ compounds doped with Mn up to 1% wt were paramagnetic. Fig. 12 demonstrate $M(T)$ curves for single crystal CdGeAs₂ doped with Mn 0.89 wt% (sample #D2) and 0.006 wt% (sample #D1). For sample #E2 $M(T)$ obeys the Langeven function

$$M = M_0 \left(\coth \left[\frac{\mu B}{kT} \right] - \frac{k_B T}{\mu B} \right), \quad (2)$$

with the mean magnetic moment of clusters $\mu = 7.1 \mu_B$ and a specific magnetization $M_0 = 1.1$ emu/g. For polycrystalline sample #C2 these values were $\mu = 6.6 \mu_B$ and $M_0 = 1.3$ emu/g. It is in good agreement with results of Ref. 86 when $\mu = 7.1 - 8.0 \mu_B$ was obtained for CdGeAs₂ doped with Mn from 0.5 up to 6 wt%. The magnetic moment of uncoupled Mn²⁺ ion is $\mu(\text{Mn}^{2+}) = 5 \mu_B$. For sample #D1 with weak paramagnetic signal (Fig. 12, Inset) we measure the electron paramagnetic resonance spectra at $T = 12$ K (Fig. 13). Six-line structure of uncoupled Mn²⁺ ions was observed with a broad signal of cation vacancy.

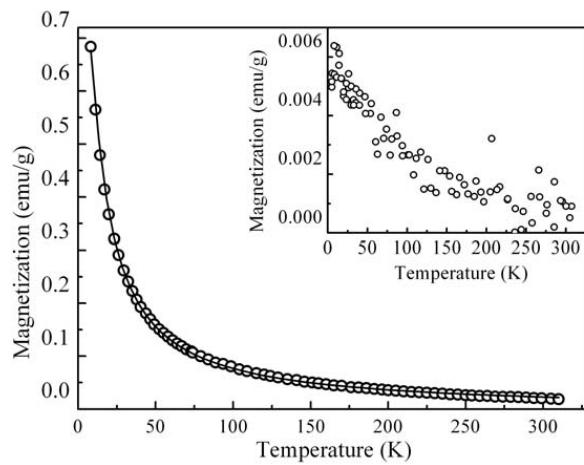


Fig.12. The temperature dependence of magnetization $M(T)$ of sample #D2 in 50 kG. The continuous line represent the Langevin function (Eq. 2) with fitting parameter given in the text. Inset: The temperature dependence of magnetization of sample #D1 in 50 kG.

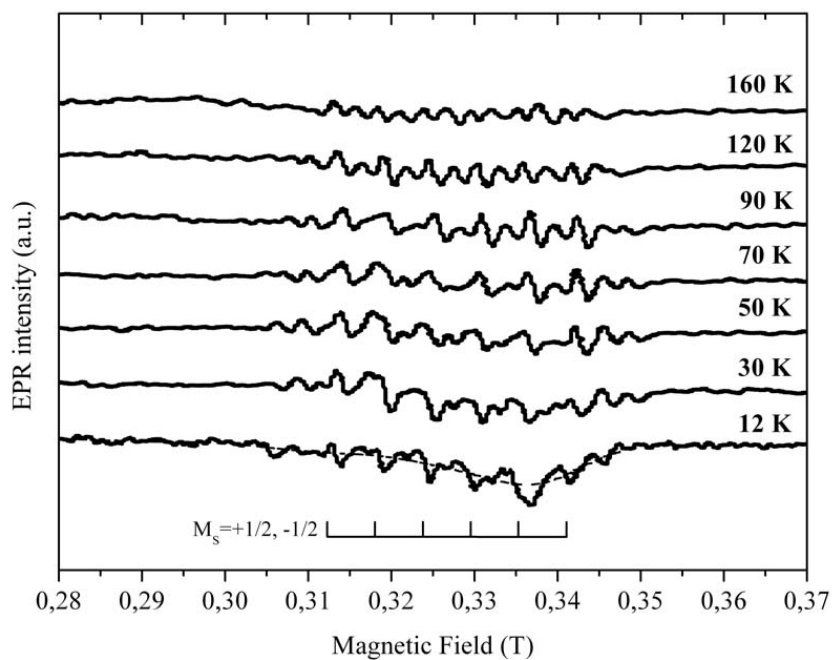


Fig. 13 EPR spectra of sample #D1 at different temperatures.

There were no signs of Mn^{4+} centers which can have $\mu = 7 \mu_B$. According to XRD analyze these centers are not formed in CdGeAs_2 samples with Mn content 1 wt% or less.

The value of $\mu > 5 \mu_B$ can be observed in p – type magnetic semiconductors with Mn^{2+} centers. In these materials the magnetic moments of the embedded Mn ions strongly interact with the magnetic moments of the charge – carrier holes. A high value of the pd -exchange constant J_{pd} (> 1 eV) leads to a considerable increase of the magnetic moment of the Mn ion in an external magnetic field [87]:

$$\mu = 5\mu_B \left(1 + \frac{J_{pd}}{\mu_B B} s \nu p \right) \approx 7\mu_B \quad (3)$$

where $s = 1/2$ is hole spin, $\nu = 0.4 \cdot 10^{-21} \text{ cm}^3$ is volume of the crystal lattice, and $p \approx 5.5 \cdot 10^{17} \text{ cm}^{-3}$ is the hole concentration of single crystal sample.

This explanation is not applicable for complex system with high concentrations of Mn ions, charge carriers and ferromagnetic clusters, observed for Mn-doped Si/ZnSiAs_2 heterostructure (Fig 9b). The behavior of the magnetization curve in this case can be explained by co-existence of two magnetic phases in the sample. The first is a ferromagnetic, M_{FM} , formed by MnAs clusters. The second one is a paramagnetic-like phase with magnetization M_{PM} described by Eq. 2. So total magnetization is

$$M = M_{PM} + M_{FM}. \quad (4)$$

With increasing the temperature $M_{PM} \rightarrow 0$ and at high temperatures $M \approx M_{FM}$. Furthermore at high temperatures the magnetization is saturated in the fields above 10 kG (Fig.14). Therefore the temperature dependence of the saturation magnetization of MnAs $\sigma_s(T)$, can be used to divide the PM and FM parts of the magnetization. $\sigma_s(T)$ was found by interpolation with a rational beta-spline function taking the basic data from Ref. 81 and by linear extrapolation at low temperatures. As shown in Fig. 9b, M_{PM} can be accurately reproduced by the Langeven function (Eq.2) with fitting parameters: $M_0 = 14.2 \pm 0.3$ a.u. and $\mu = 7.6 \pm 0.2 \mu_B$ [**publication 4**]. The last value is very close to magnetic moment obtained for Mn-doped CdGeAs_2 crystals.

To make clearer the reasons of exceeding of $\mu(\text{Mn}^{2+})$ in different material we estimate the effective number of Bohr magnetons per Mn ion, p_{eff} , in $\text{Zn}_{0.9}\text{Cd}_{0.1}\text{GeAs}_2\text{:Mn}$. In the field $B = 50$ kG the contribution of the MnAs clusters to ferromagnetic magnetization $M_{FM} = \eta \varphi \sigma_s(T)$, is practically saturated while the paramagnetic magnetization of free Mn ions $M_{PM}(T) \approx \chi_{PM}(T)B$ is still sufficiently far from saturation. Here $\varphi = 4.84 \text{ g}\cdot\text{cm}^{-3}$ is the density and $\chi_{PM}(T) =$

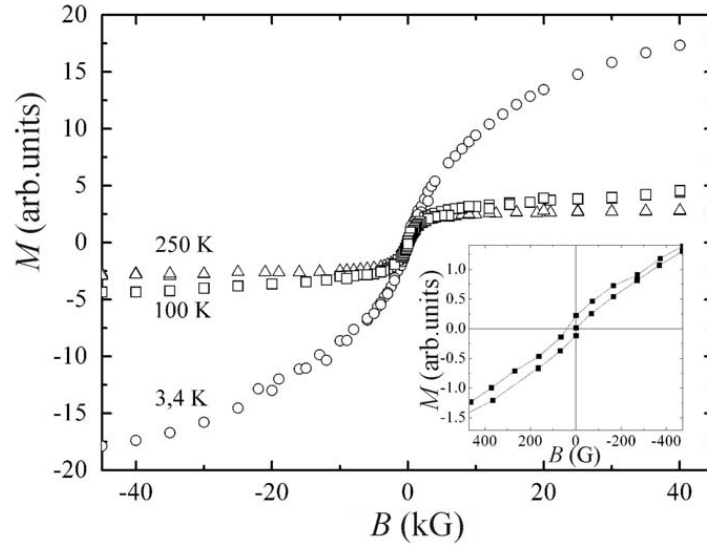


Fig.14. Magnetization $M(B)$ for Mn-doped Si/ZnSiAs₂ heterostructure. Inset: part of the low-field hysteresis loop measured at $T = 3.4$ K [publication 5].

$= C/(T-\theta_{CW})$, where $C = p_{eff}^2 \mu_B N_{Mn} / 3k_B$ is Curie constant, N_{Mn} is the concentration of Mn outside the MnAs clusters and θ_{CW} is the Curie – Weiss temperature. From the best fit of $M(T)$ we obtain values of $p_{eff}^2 \approx 20$ and 25 for samples #B2 and #B3, respectively, which are smaller than the effective Bohr magneton number for free Mn²⁺ ($p_{eff}^2 \approx 35$) [Publication 2]. Such p_{eff}^2 reduction can be explained by forming of Mn complexes, especially dimmers and trimmers. Theoretical calculations performed for (Ga,Mn)As system showed the possibility of Mn clustering into stable and electronically active dimmers, trimmers or tetramers [88]. Such complexes was observed in InMnAs [89], (In,Mn)Sb epitaxial films [71] and Ge:Mn [90]. In these complexes Mn atoms placed on the positions in neighbor unit cells and interact antiferromagnetically. Therefore their effective magnetic moment is reduced. Mn atoms from complexes interact with other type atoms too, especially with As. So the most probable value of μ for Mn atoms is close to $\mu(\text{MnAs})$ which is $3.4 \mu_B$ [91]. The value of magnetic moment $\approx 7 \mu_B$ supports of the assumption that most of Mn atoms in lattice form dimmers.

InMnSb

As mentioned above, one of specific features on the $M(T)$ curves of InMnSb samples is the increasing of $M(T)$ at $T \rightarrow 0$ in the range $T < 20$ K (Fig. 11a). Curves with $M(T)$ rising at $T \rightarrow 0$ were observed also in other Mn-doped III-V compounds [42, 71]. In InMnSb the low temperature increase of $M(T)$ is attributed to the FM transition in the matrix caused by Mn atoms

placed in In positions. This was observed earlier in MBE grown InMnSb films [66, 92] and in our samples it occurs at $T < 20$ K.

Similar to II-IV-As₂, the behavior of $M(T)$ in InMnSb can be explained by co-existing of two magnetic phases: the para- or superparamagnetic-like magnetization M_{PM} and the ferromagnetic M_{FM} of MnSb clusters. We can rewrite the Eq.4 for total magnetization

$$M = M_{PM} + M_{FM} = M_{PM0} \left(\coth \left(\frac{\mu B}{k_B T} \right) - \frac{k_B T}{\mu B} \right) + \eta M_{MnSb}(T), \quad (5)$$

where $M_{PM0} = n_{PM}\mu$ is the specific magnetization of paramagnetic subsystem, n_{PM} is the concentration of superparamagnetic particles, μ is the effective magnetic moment of a particle, η is the mass fraction of MnSb and $M_{MnSb}(T)$ is the temperature dependence of the saturation magnetization of MnSb. We found $M_{MnSb}(T)$ by interpolation with a rational beta-spline function using the basic data from Ref. 83.

At high temperatures $M \approx M_{FM} = \eta M_{MnSb}(T)$. This allow to estimate η for all samples and use only two parameters M_{PM0} and μ for fitting $M(T)$ using eq. (5). Results are shown as solid lines in Fig. 11a with fitting parameters and some other calculated values presented in the Table 5.

Table 5. Parameters of InMnSb samples [**Publication 6**].

	Mn, wt%	Mn content, x	η , wt%	η , Vol. %	M_{PM0} , emu/g	μ , μ_B	n_{PM} , cm ⁻³
1	0.12	0.005	0.3	0.25	0.11	8.4±0.4	8.2·10 ¹⁸
2	0.5	0.02	1.2	1.0	0.28	8.8±0.4	1.9·10 ¹⁹
3	0.7	0.03	1.85	1.6	0.36	9.4±1.2	2.4·10 ¹⁹
4	1.4	0.06	4.1	3.5	0.41	8.1±0.4	3.2·10 ¹⁹

The small η value is consistent with Fig.5 where one can see that MnSb grains (black dots in Fig. 5a) occupy only a small part of the sample volume. Having η value and the amount of Mn used in technological process we estimated the concentration of Mn atoms incorporated into InSb lattice n_{Mn} . Because η increases nonlinearly with Mn content, n_{Mn} tends to saturate as seen in Fig. 15. For our growth method of InMnSb we estimated the solubility limit of Mn as $\sim 10^{20}$ cm⁻³. This value is about one order of magnitude more than solid solubility of Mn in bulk InSb crystals, $5 \cdot 10^{18} - 1 \cdot 10^{19}$ cm⁻³ [63], but 5 times less than Mn content in In_{1-x}Mn_xSb epitaxial films [71].

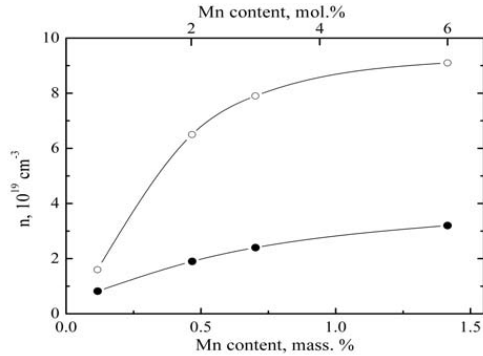


Fig. 15. Concentrations of Mn atoms substituting In in the InMnSb lattice n_{Mn} (open circles) and of paramagnetic particles n_{PM} (solid circles) as the function of Mn content [Publication 6].

The temperature dependences of paramagnetic part of magnetization $M_{\text{PM}}(T)$ are illustrated in Fig. 16. As it is seen from inset $M_{\text{PM}}^{-1}(T)$ follows Curie law proving its para- or superparamagnetic nature. Dashed lines in the inset are guides for eyes. In this figure the data obtained at $T \leq 10$ K are omitted because the

$$\text{coth } y = \frac{1}{y} + \frac{y}{3} - \frac{y^3}{45} + \dots$$

leading to the Curie or Curie-Weiss law is valid only for $y \ll 1$. Also, just close to this temperature the FM transition inside InMnSb matrix could occur [66, 92].

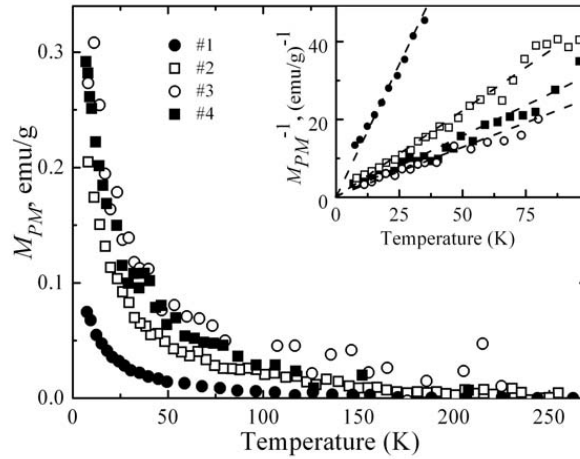


Fig. 16. Paramagnetic contribution M_{PM} to the sample magnetization without high temperature ferromagnetic part M_{FM} . Different symbols correspond to different samples. The inset shows $M_{\text{PM}}^{-1}(T)$ which follows the Curie law. Lines are guide for eye [publication 6].

Concentration of paramagnetic particles n_{PM} is about 10^{19} cm^{-3} and its magnetic moment is about $9\mu_{\text{B}}$ (see Table 5). Normally, μ of Mn^{2+} ($S = 5/2$) occupying an In site is about $5\mu_{\text{B}}$. Such values were found in $\text{In}_{1-x}\text{Mn}_x\text{Sb}$ epitaxial films [66]. It is about 2 times smaller than the magnetic moment of paramagnetic particle found in our case and presented in the Table 5. We take into account the small concentration of single-domain MnSb clusters, the absence of other

clusters detected by AFM, SEM, NMR and X-ray studies and the small magnetic moment of isolated Mn ions. In this case it is naturally to suggest that clusters of atomic size or complexes mentioned above is the reason for paramagnetic contribution at $T \leq T_C$ and the enhanced μ value. On the other hand n_{PM} is about 3 times less than n_{Mn} (Fig. 15). That also proves the assumption of the availability of Mn complexes, especially dimmers and trimmers. For sample #4 $n_{Mn} \approx 9 \cdot 10^{19} \text{ cm}^{-3}$ while $n_{PM} = 3.2 \cdot 10^{19} \text{ cm}^{-3}$. Taking into account that not all Mn atoms entering In sites form such complexes it is reasonable to suggest that mainly dimmers act as such complexes. Moreover some of Mn atoms inside InSb lattice are magnetically inactive. This also decreases the n_{PM}/n_{Mn} ratio. The value of magnetic moment $\approx 9\mu_B$ also supports of the assumption that most of complexes are dimmers.

3.4 Nanosize MnAs and MnSb precipitations

II-IV-As₂:Mn

Presence of nanosize MnV precipitations was observed by magnetic measurements at low magnetic fields. $M(T)$ dependences of II-VI-As₂:Mn measured in ZFC and FC regimes are shown in Fig.17.

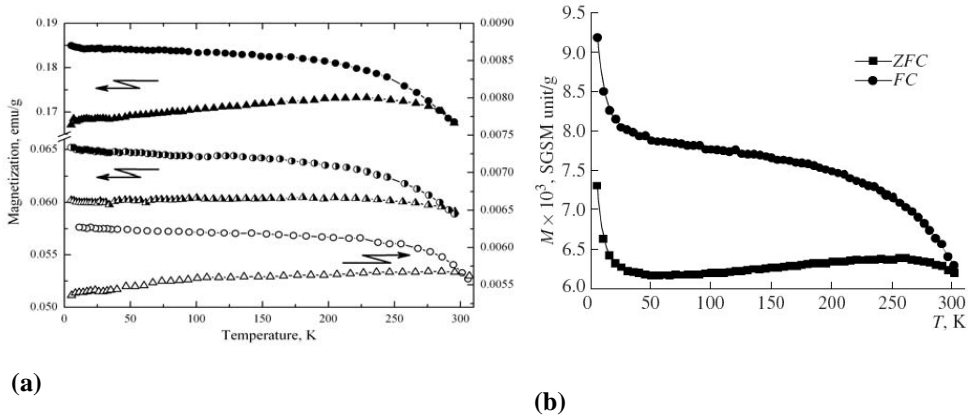


Fig. 17. Temperature dependences of magnetization, measured in low magnetic fields: (a) M_{ZFC} (triangles) and M_{FC} (circles) for $Zn_{0.9}Cd_{0.1}GeAs_2:Mn$ sample #B2 (open symbols), sample #B3 (half-filled symbols) at $B = 5$ G and sample #B3 (solid symbols) at $B = 50$ G [publication 2]; (b) $ZnSiAs_2:Mn$ sample #E3 at $B = 100$ G [publication 5].

The difference between the M_{FC} and M_{ZFC} curves decreased with increasing the field (Fig.17a) and disappeared at $B > 10$ kG. A broad maximum of the $M_{ZFC}(T)$ curves was observed around $T_b \approx 250$ K both for $Zn_{0.9}Cd_{0.1}GeAs_2:Mn$ and $ZnSiAs_2:Mn$ samples.

Magnetic properties of II-VI-As₂Mn are determined mostly by small ferromagnetic MnAs clusters. At $T > T_b$ or above the blocking temperature such clusters exhibit superparamagnetic behavior because of the thermal fluctuations. At $T < T_b$ the magnetic moments of the particles are blocked, with their directions distributed at random over the sample volume. In this case the source of the blocking barrier is the anisotropy energy of individual particles [93]. The moment of each particle is stabilized independently when anisotropy energy KV (K is the density of the anisotropy energy and V is the average volume of the particles) becomes enough to counteract the thermal excitations about $k_B T$. After removal of the external field the moments of the particles relax towards equilibrium state. If relaxation time 10^2 s is used as the criterion for transition to stable state, the energy barrier must be $25 k_B T$. Then the blocking temperature of FM particles is [94]

$$T_b = \frac{KV}{25k_B}. \quad (6)$$

The susceptibility of a system of arbitrary clusters can be written in the form [93]

$$\chi_{ZFC}(T) = \chi_0 + \frac{C}{T} \int_0^T f(T_1) dT_1, \quad (7)$$

where χ_0 is χ_{ZFC} at $T < T_b$, and $\chi_{ZFC} = C/T$ at $T > T_b$, C is Curie constant for clusters and $f(T)$ is the distribution function of the blocking temperatures. One must use a small magnetic field during measurements to avoid the influence of stable ferromagnetic (nonsuperparamagnetic) clusters on the susceptibility. The low-field contribution to χ from such kind of clusters is small and depends on T only via σ_s . So the first term in Eq.7 represent the contribution of stable clusters and the second term correspond to contribution of superparamagnetic clusters. Parameters χ_0 and C depends only on σ_s and can be express as $\gamma\alpha\sigma_s^2$ and $\gamma\sigma_s^2$, respectively (α and γ are constants). Then Eq.7 can be written as [93]

$$\chi_{ZFC}(T) = \gamma\sigma_s^2 \left(\alpha + \frac{1}{T} \int_0^T f(T_1) dT_1 \right). \quad (8)$$

After differentiation of Eq.8 with respect to T the $f(T)$ can be found as [93]

$$f(T) = \frac{1}{\gamma} \frac{d}{dT} \left(\frac{\chi_{ZFC} T}{\sigma_s^2} \right) - \alpha. \quad (9)$$

Eq.9 and Eq.6 gives possibility calculate in a numerical form the distribution function $f(r)$ of the radius of the sphere corresponding to the cluster volume $V = \frac{4}{3}\pi r^3$. The temperature dependences of K and σ_s for MnAs were taken from the Ref. 81 and used in interpolation with a rational beta-spline function. Low temperature parts of $K(T)$ and $\sigma_s(T)$ were found by linear

extrapolation. The constants λ and γ were determined by normalizing $f(r)$ to unity and using the condition $f(r)=0$ at $r=0$. Fig. 18 demonstrate $f(r)$ curves for different II-VI-As₂:Mn compounds. Fitting $f(r)$ with Gaussian function:

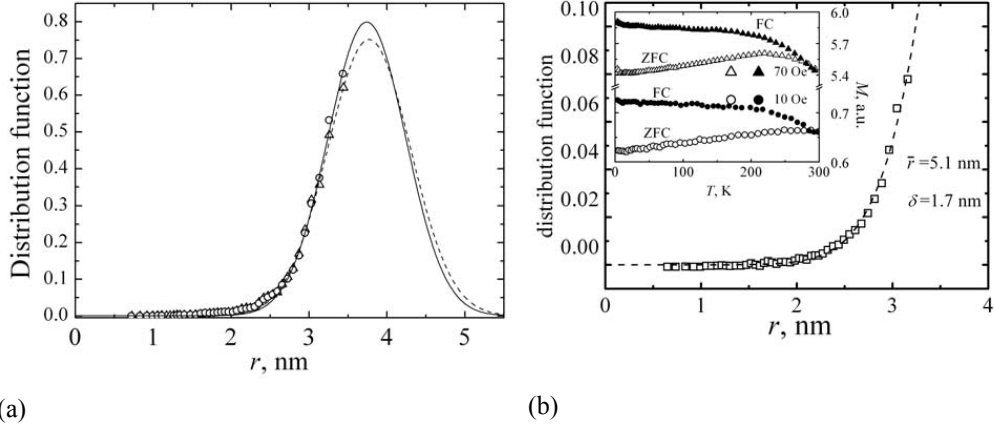


Fig. 18. The distribution function of the magnetic cluster radius calculated with Gaussian function (Eq.10) for samples: (a) Zn_{0.9}Cd_{0.1}GeAs₂:Mn #B2 (circles, dashed line) and #B3 (triangles, continuous line) [publication 2]; (b) Mn-doped ZnSiAs₂/Si heterostructure #F1, inset: magnetization as a function of temperature measured in low magnetic fields for sample #F1. Experimental data points of the distribution function are calculated using Eq. 6 and Eq. 9.

Table 6. Parameters of MnAs nanoclusters for different II-VI-As₂:Mn samples.

Sample	\bar{r} , nm	δ , nm	$\mu(300 \text{ K})$, μ_B
#B2	3.7	1.0	$1.4 \cdot 10^4$
#B3	3.8	1.1	$1.6 \cdot 10^4$
#E2	2.76	0.72	$6.0 \cdot 10^3$
	3.10	0.35	$8.5 \cdot 10^4$
#E3	3.57	0.96	$1.3 \cdot 10^4$
#F1	5.1	1.7	$3.5 \cdot 10^4$

$$f(r) = \frac{1}{\sqrt{2\pi}} e^{-\frac{(r-\bar{r})^2}{2\delta^2}} \quad (10)$$

gives the most probable radius of clusters \bar{r} and mean-square deviation δ (Table 6). The clusters magnetic moment μ (Table 6) was calculated using expression $\mu = \mu_{300 \text{ K}} \cdot V/v$ where the volume v and magnetic moment $\mu_{300 \text{ K}}$ per MnAs pair are $v \approx 34 \text{ \AA}^3$ [91] and $\mu_{300 \text{ K}} \approx 2.3 \mu_B$ [95],

respectively. Our values of μ agree with results of Ref. 96 where $\mu = (1.2 - 2.0) \cdot 10^4$ was obtained for Mn-doped ZnSiAs_2 without clear explanation about the nature of magnetic clusters. The mean cluster radius increase when increase Mn content. At low Mn concentrations (sample #E2) $f(r)$ has more complex character and is described by sum of two Gaussian functions. The same situation was observed in Ref. 93 for $\text{Zn}_{1-x}\text{Mn}_x\text{As}_2$.

InMnSb

The difference between the M_{FC} and M_{ZFC} curves point out on existing of superparamagnetic clusters in InMnSb samples (Fig. 11b) with $T_b \sim 500$ K. Using general formulas for blocking temperature of superparamagnetic particles (Eq. 6) and anisotropy parameters for MnSb [82] we estimated that to have T_b near 500 K the diameter of particles $d \approx 20$ nm is required. Therefore superparamagnetic contribution to the magnetization in InMnSb samples could originate from single-domain MnSb clusters with diameter less than 20 nm. It is in good agreement with AFM investigations (Fig. 5b) which gave the mean diameter of MnSb clusters to be 24 nm.

The existence of superparamagnetic particles in our samples is supported also by field dependences of magnetization, $M(B)$, shown in Fig. 19 for sample #4 at various temperatures. One can see that at high magnetic fields saturation of magnetization is not complete and $M(B)$ looks like the one for superparamagnetic materials. For other samples the behavior of $M(B)$ is similar. However, the magnetic field dependence of magnetization $M(B)$ could not be described only by classical model of superparamagnetism (for example, by Langevin equation), because all $M(B)$ curves do not merge with B/T scaling. Observation of the hysteresis reveals the presence of the FM contribution related to sufficiently large MnSb inclusions. Coercive force B_C was found to be about 100 G at 5 K (Fig 19, inset) and it decreases slightly with temperature increase (70 G at 510 K). The coercive force could be estimated as $B_C \approx \frac{4\pi}{3} M_s$, where M_s is the saturation magnetization of FM subsystem and giving $B_C \approx 75$ G at 5 K and 50 G at 510 K. This is in reasonable agreement with experimental values. For samples #A3 and #A4 the coercive force was about 50 G. It is known that samples containing MnSb particles with mean diameter ~ 15 and 30 nm exhibit FM behavior with $B_C \sim 6500$ and 4500 G, respectively [57] and $B_C \sim 300$ G for micrometer size particles [97]. Lower coercivity in our samples is due to very weak coupling between ferromagnetic MnSb particles because their concentration in samples is about 10^{15} cm^{-3} .

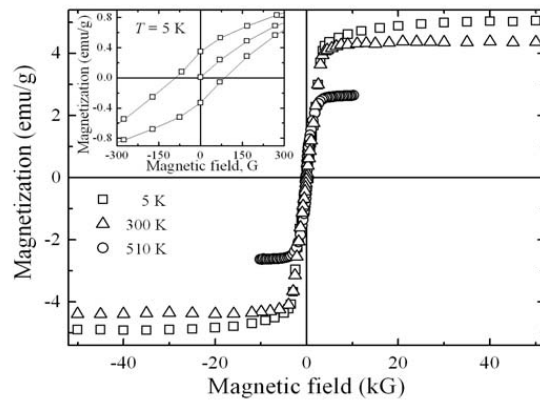


Fig. 19. Magnetization function $M(B)$ for sample #A4 measured at $T = 5$ K, 300 K and 510 K. Inset: parts of the low field hysteresis loops at 5 K [**publication 6**].

4 Transport properties of InSb and II-IV-As₂ semiconductors doped with Mn

4.1 Experimental procedure

The electrical and magnetotransport properties of samples were investigated between 1.6 K and 320 K using the standard six-point geometry, where the four side contacts allow the simultaneous measurement of the longitudinal and the transverse voltage. The samples with the dimensions $5 \times 1 \times 0.1 \text{ mm}^3$ were cut from crystals by Abrasive Slurry Saw – *Model 850 (South Bay Technology Inc.)*.

A pulse magnet solenoid was used to generate a strong magnetic field pulse up to 250 kG with the pulse duration about 10 ms. Low - field investigations were executed with a dc superconducting solenoid. In all measurements the magnetic field was applied perpendicularly to the largest face of the sample. Contacts to the samples were prepared by soldering with tin-and-lead solder. The resistance was measured with a high accuracy (the error was at most 1% of the measured value). The samples had high conductivity and linear current–voltage characteristics in the range of the measurements.

4.2 Temperature dependence of resistivity

InMnSb

Figs. 20 and 21 display resistivity ρ versus temperature for InMnSb samples. Two feature of the

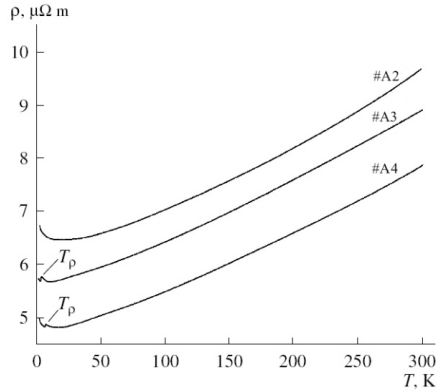


Fig. 20. Resistivity vs. temperature curves for InMnSb samples [publication 1].

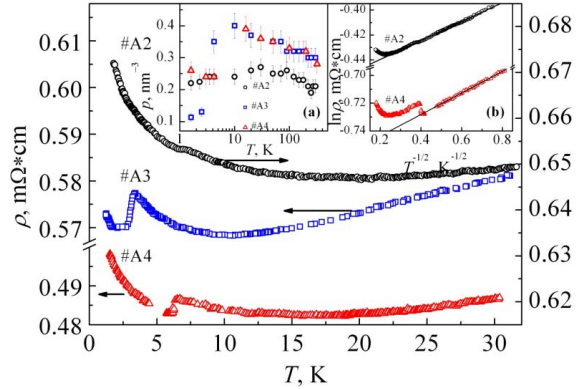


Fig. 21. Temperature dependence of zero-field resistivity ρ for InMnSb samples. The inset (a) show temperature dependences of hole concentration. The inset (b) shows the $\ln \rho$ vs $T^{-1/2}$ for samples #A2 and #A4 [publication 6].

resistivity curves are clear visible.

First, a semiconductor - like activated character of specific resistance was observed at low temperatures. As temperature increased (at $T > 15 - 20$ K), it changed to a metallic resistivity with smooth increasing of ρ . This is intrinsic to good conductors with magnetic impurity. The increase of the specific resistance $\rho(T)$ at temperatures below the minimum $\rho(T)$ correlates with decreasing hole concentration (see Fig.21, inset (a)), especially in the samples with high Mn concentration. This may be connected to trapping of holes at interfaces between the MnSb clusters and the InMnSb matrix as observed for paramagnetic-ferromagnetic GaAs:Mn/MnAs hybrids [98]. Plots of $\ln\rho$ vs $T^{-1/2}$ at lowest temperatures ($T < 7$ K) (Fig. 21, inset (b)) can be best fitted with T^{-m} -type functions ($m = 1, 1/2, 1/3$ and $1/4$). The $T^{-1/2}$ law has been observed for many composite materials including granular metals, digital alloys and heavily doped semiconductors [99]. According to Zvyagin and Keiper model [100], for granular materials the main mechanism of conductivity is the variable range hopping between grains located far away from each other. To make such hops real is needed that the electron path from an initial granule to the final includes tunneling between grains and also electrons transport through virtual states in intermediate granules (in granules located between initial and final those). Similar transitions through real states are extremely improbable due to the big difference between energies of these states, so electron should get energy of a big value for such transition. Therefore the temperature at which such transitions could be possible exceeds many times over the temperature of measurements. For the polycrystalline InMnSb with micrometers size MnSb microcrystallites the increase of the resistivity at the low temperatures was observed by Ganesan et.al. [50] with dominating Mott's variable range-hopping mechanism i.e. « $T^{-1/4}$ -law». This behavior was explained by strong localization of carriers on impurity sites and on the interface between the MnSb clusters and the semiconducting matrix, and by thermal activation of the charge carriers from a reservoir into the transport-carrying band states. This is possible if the energy distribution of reservoir states is sufficiently broad or the density of band states exhibits tails.

Second, $\rho(T)$ for samples #A3 and #A4 have small peaks at $T < 7$ K (Fig. 21). The resistivity typically exhibits a peak or shoulder near the ferromagnetic transition temperature for both insulating (peak) and metallic (shoulder) samples [101]. It is important to note that existence of this peak in the vicinity of T_c was also found in ferromagnetic $\text{In}_{1-x}\text{Mn}_x\text{Sb}$ films grown by MBE [66, 102]. The non-monotonic behavior of $\rho(T)$ near T_c in DMS is usually associated with critical scattering. This is predicted by scaling theory of magnetotransport in Anderson-localized disordered ferromagnets due to interplay between magnetism and disorder near the magnetic phase transition [103]. In our samples the peak in $\rho(T)$ can be attributed to

low-temperature ferromagnetic phase with $T_c < 3$ K for sample #A3 and $T_c < 6$ K for sample #A4. The existence of this peak and FM transition inside the matrix reveal the role of the Mn atoms entered the In positions in our InMnSb samples.

For our case the matter is that the FM transition occurs in the range of hopping conductivity when there are no free electrons for Ruderman-Kittel-Kasuya-Yosida exchange mechanism. However, it is not something new and surprising. The FM ordering under insulating regime were already discussed in various materials [104] in particular in bulk GaMnAs [105], 2D GaMnAs structures [106] and Ge:Mn [107]. The reasons for the non-monotonic $\rho(T)$ behavior are the same as in metallic samples if instead of scattering the tunneling will be taken into account. It should be mentioned that both magnetization and transport properties observed in Ge:Mn [107] are very similar to those revealed in our samples. The nature of the exchange in samples with nonmetallic conductivity is discussed and related either to carriers localized in the impurity band, or to the bound magnetic polaron percolation model of ferromagnetism [107, 108].

II-IV-As₂:Mn

Fig 22 shows the temperature dependences of resistivity of Zn_{1-x}Cd_xGeAs₂:Mn samples. Only the single crystal (Fig.22b) has $\rho(T)$ dependence characteristic to the nondegenerated semiconductor. The $\rho(T)$ curve of polycrystalline sample #B3 heavily doped with Mn has a large maximum at $T \approx 170$ K. $\rho(T)$ curve of undoped sample #B1 coincide with the curve of Mn-doped sample #B2 at $T > 40$ K. So the influence of magnetic precipitation on resistance at high

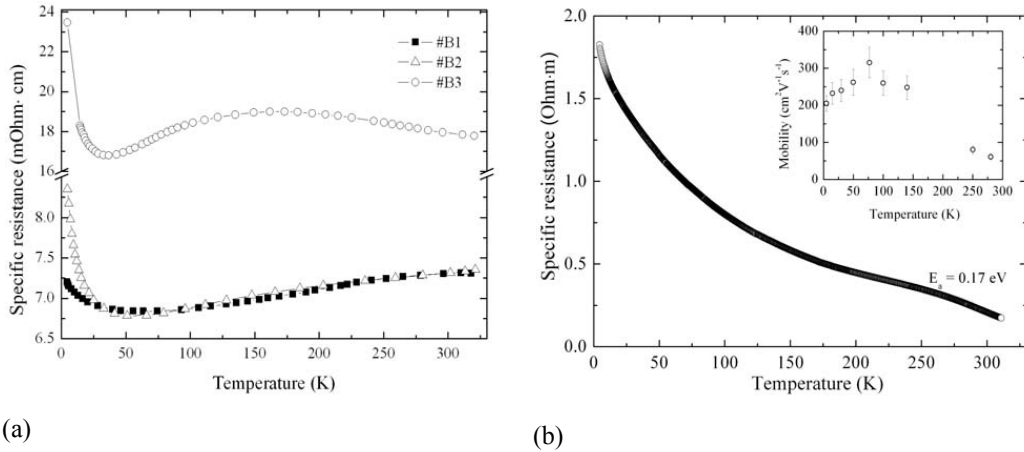


Fig. 22. The temperature dependence of resistivity of Zn_{0.9}Cd_{0.1}GeAs₂:Mn polycrystalline samples (#B1, #B2, #B3) (a) and CdGeAs₂:Mn single crystal sample #D1 (b). Inset shows temperature dependence of carrier mobility in sample #D1.

temperatures is small. Samples had p-type conductivity with charge carrier concentration $p_2 = 1.4 \cdot 10^{20} \text{ cm}^{-3}$ and $p_3 = 1.0 \cdot 10^{20} \text{ cm}^{-3}$ at $T = 4.2 \text{ K}$ for #B2 and #B3, respectively. With increasing temperature to 300 K these values slowly increased to $p_2 = 1.9 \cdot 10^{20} \text{ cm}^{-3}$ and $p_3 = 1.3 \cdot 10^{20} \text{ cm}^{-3}$. The hole mobility μ_p for all samples was about $10 - 20 \text{ cm}^2/(\text{V}\cdot\text{s})$ and decreased slowly when temperature increased.

The $\rho(T)$ for sample #D1 with low Mn concentration has a semiconductor character (Fig. 22b). At $T > 250 \text{ K}$, this dependence is indicative of the presence of an acceptor level with the activation energy $E_a = 0.17 \text{ eV}$. This is consistent with the energy of 0.175 eV observed in the study of CdGeAs_2 single crystals Mn-doped with 6 mass.% [109]. The hole concentration increased from $1.6 \cdot 10^{14} \text{ cm}^{-3}$ to $4.5 \cdot 10^{15} \text{ cm}^{-3}$ as the temperature raised from 4.2 to 320 K. The character of the temperature dependence of the hole mobility μ_p (Fig. 22b, inset) is similar to that observed in many semiconducting compounds. The hole mobility changes from $60 \text{ cm}^2/(\text{V}\cdot\text{s})$ at 280 K to $320 \text{ cm}^2/(\text{V}\cdot\text{s})$ at 80 K. In Ref. 110 has been demonstrated that the maximum mobility in CdGeAs_2 (a polycrystalline sample) doped with 3 mass.% Mn is observed at 175 K. The presence of the maximum at $\sim 80 \text{ K}$ (Fig. 22b, inset) in sample #D1 shows that the impurity contribution still plays an important role in charge-carrier scattering in Mn doped CdGeAs_2 .

4.3 Magnetoresistance and low-temperature ferromagnetic ordering

InMnSb

In Fig. 23 are shown typical magnetic field dependences of the magnetoresistance $\Delta\rho/\rho = (\rho_B - \rho_0)/\rho_0$ at different temperatures for InMnSb samples (here ρ_B and ρ_0 are resistivities in nonzero and zero magnetic fields, respectively). In sample #A4 maximal negative magnetoresistance $\Delta\rho/\rho = -16.3 \%$ is observed at $T = 1.6 \text{ K}$. At $T < 10 \text{ K}$ $\Delta\rho/\rho$ is negative up to 40 – 90 kG and has an upturn due to the positive classical contribution in increasing magnetic fields.

Reasons for negative magnetoresistance are quantum corrections to conductivity [111] and the magnetic nature (spin dependent scattering or tunneling of carriers). The existence of the quantum corrections contribution to the negative magnetoresistance is supported by the observation of positive magnetoresistance at very small fields (Fig. 23, inset) and is due to strong spin-orbit interaction [111]. The negative magnetoresistance takes place at very high magnetic fields. Therefore the spin dependent scattering or tunneling should play a main role. The negative magnetoresistance in InMnSb at low temperatures may be caused by two mechanisms.

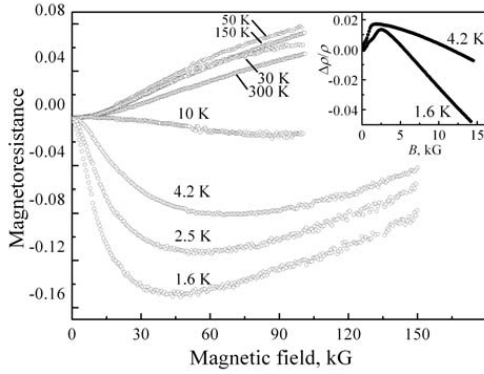


Fig. 23. Magnetic field dependence of the magnetoresistance for sample #A3 at different temperatures measured in pulsed magnetic fields. Inset: low-field part of magnetic field dependence of the magnetoresistance for sample #A4 measured using dc superconducting solenoid [publication 6].

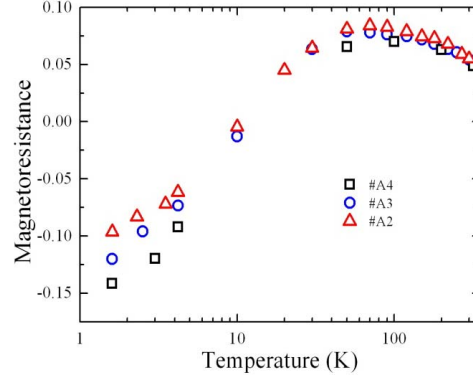


Fig. 24. Temperature dependence of the magnetoresistance for InMnSb samples at $B = 100$ kG.

First possible mechanism is that scattering of spin-polarized carriers on Mn^{2+} ions leads to decreasing of the resistivity. For InMnSb the theory of this process was elaborate in Ref. 112.

The Hamiltonian for the interaction between the spin s of delocalized holes and the spin S of $3d$ shells of the Mn ions is $H = V_{int} - 2 J_{pd} \mathbf{s} \cdot \mathbf{S}$, where V_{int} is the spin-independent part of the potential, and J_{pd} is the coupling constant. In the presence of a magnetic field the relaxation times τ_{\pm} for the spin-up and spin-down carriers are different. The relaxation time up to second order in J_{pd}/V_{int} is [112]

$$\frac{1}{\tau_{\pm}} = C_0 \left[1 \mp \frac{2J_{pd}}{V_{int}} \langle S_z \rangle + \left(\frac{2J_{pd}}{V_{int}} \right)^2 f(\langle S_z^2 \rangle) \right], \quad (10)$$

where $\langle S_z \rangle$ is the component given by the Brillouin function

$$\langle S_z \rangle = \frac{6}{5} \coth\left(\frac{6}{5}\nu\right) - \frac{1}{5} \coth\left(\frac{1}{5}\nu\right), \quad (11)$$

with argument $\nu = g\mu_B B / (k_B T_{eff})$. The tabulated values of $f(\langle S_z^2 \rangle)$ and C_0 are given in Ref. 113.

Corresponding magnetization in this notes is $M = g\mu_B \langle S_z \rangle$.

In the range of $T < T_C$ the ferromagnetically ordered regions increase but some Mn^{2+} spins can still remain outside the ferromagnetic network and cause magnetic scattering. In this case the magnetoresistance is proportional both to spin polarization P , arising from the

ferromagnetic regions, and to ordering of the isolated paramagnetic moments [112]. This can be written as

$$\frac{\Delta\rho}{\rho} = -4P \frac{J_{pd}}{V_{\text{int}}} \langle S_z \rangle = -4P \frac{J_{pd}}{g\mu_B V_{\text{int}}} M(B). \quad (12)$$

Effective temperature in this case is $T_{\text{eff}} = T + T_{AF}$, where T_{AF} is the empirical antiferromagnetic coupling parameter. At $T > T_C$, the ferromagnetic phase becomes paramagnetic and the magnetoresistance is expressed by [112]

$$\frac{\Delta\rho}{\rho} = -\frac{J_{pd}^2}{V_{\text{int}}^2} \left[4\langle S_z \rangle^2 + \langle S_z \rangle \left(\coth\left(\frac{\nu}{2}\right) - \frac{\nu}{2 \sinh^2\left(\frac{\nu}{2}\right)} \right) \right], \quad (13)$$

with $T_{\text{eff}} = T - T^*$, where T^* is usually close to T_C . When the ferromagnetic ordering changes to paramagnetic the dependence $\frac{\Delta\rho}{\rho}$ on $\langle S_z \rangle$ turns to quadratic one.

The second possible mechanism for the negative magnetoresistance in our samples is nano-scaled MnAs clusters embedded in the GaAs:Mn matrix which is similar to that used for granular paramagnetic-ferromagnetic GaAs:Mn/MnAs hybrid layers [103]. In general, the magnetoresistance in these systems is controlled by competition of the negative and positive terms while the paramagnetic matrix plays a significant role. At low temperatures in zero external magnetic field the holes are trapped near the cluster interface due to local Zeeman splitting and they form bound magnetic polarons together with the hole concentration. This is decreasing upon cooling the sample. At $B_{\text{ext}} = 0$ the giant Zeeman splitting spreads into the paramagnetic GaAs:Mn matrix resulting in aligning of the carrier spins and negative magnetoresistance. With increasing temperature both Zeeman splitting and the trapping depth will change following the Brillouin function $\langle S_z \rangle$ [98]. The positive part of the magnetoresistance in granular paramagnetic-ferromagnetic systems arises from different spin orientations of the clusters and the majority of the carriers. At higher temperatures thermal disorder destroys the preferential spin orientation of the Mn ions, decreasing the positive magnetoresistance. In principle MnSb clusters contribute to the negative magnetoresistance in InMnSb as it was observed for MnAs clusters in GaAs:Mn [98]. In general, the magnetoresistance in these systems is controlled by competition of the negative and positive terms while the paramagnetic matrix plays a significant role. When the temperature increases, the negative magnetoresistance decreases rapidly. Eventually $\frac{\Delta\rho}{\rho}$ becomes positive reaching a

maximum $\frac{\Delta\rho}{\rho} = 8.4\%$ at $T \approx 70$ K for sample #A4. Above 70 K it slowly decreases (Fig. 24).

Similar behavior was observed for (In,Mn)Sb crystals containing MnSb micro clusters [50] and for GaAs:Mn/MnAs [43, 98].

Both of the above mechanisms are important in forming of the negative magnetoresistance in our samples at low temperatures.

However, the concentration of MnSb clusters (about $2 \cdot 10^{15} \text{ cm}^{-3}$) in our case is much smaller than n_{Mn} and n_{PM} . So their role for spin dependent scattering or tunneling should be rather small compare to that described by Eq. (12) and (13). In spite of MnSb nanograins volume fraction is 3.5% the number of MnSb nanograins is small because of their big volume with their averaged size 24 nm (see Fig. 5b). This statement is supported by the observation that the negative magnetoresistance takes place only at temperatures lower or close to T_{Cm} related to the FM transition in the InMnSb matrix. So for negative magnetoresistance the main contribution at low temperatures is coming from the spin-dependent scattering or tunneling of carriers between magnetic moments inside matrix. Because the main mechanism of conductivity in this temperature range is hopping, the spin-dependent tunneling should be the main reason for negative magnetoresistance. According Eq. (12) and (13) $\frac{\Delta\rho}{\rho} \propto M$ for FM state and $\frac{\Delta\rho}{\rho} \propto M^2$ for paramagnetic state. Here we believed that $\langle S_z \rangle$ is proportional to M . Taking that into account we can estimate the temperature dependence of magnetization $M_{\text{eff}}(T)$ obtained from $\frac{\Delta\rho}{\rho}(T)$ at low temperatures. Here the positive magnetoresistance was subtracted because it depends weakly on temperature in the range 30 – 150 K as it is seen from Fig. 23. It should be mentioned that calculated $M_{\text{eff}}(T)$ value is related to the magnetic moments inside the InMnSb matrix, but it does not take into account the magnetization of big MnSb clusters. It is relevant to the assumption that these clusters do not contribute essentially to the negative magnetoresistance. The calculated $M_{\text{eff}}(T)$ is presented in Fig. 25 for samples #A2 and #A4. It is seen that for sample #A2 the obtained $M_{\text{eff}}(T)$ coincide with $M_{\text{PM}}(T)$ which is the calculated paramagnetic contribution to $M(T)$ obtained from the magnetometry data. For sample #A4 $M_{\text{eff}}(T)$ deviate at $T < T_{Cm}$ from this extrapolation to higher values. This is in agreement with observation of low-temperature peak at $\rho(T)$ for the sample #A4 and it's absence for the sample #A2. This proves the FM transition but only for sample #A4.

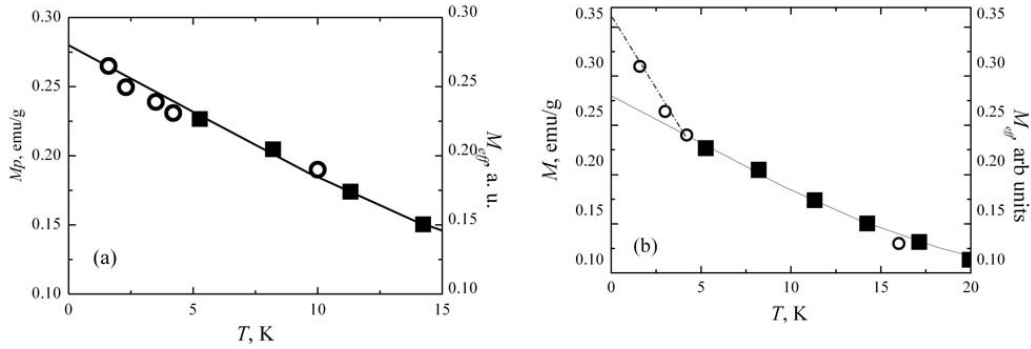
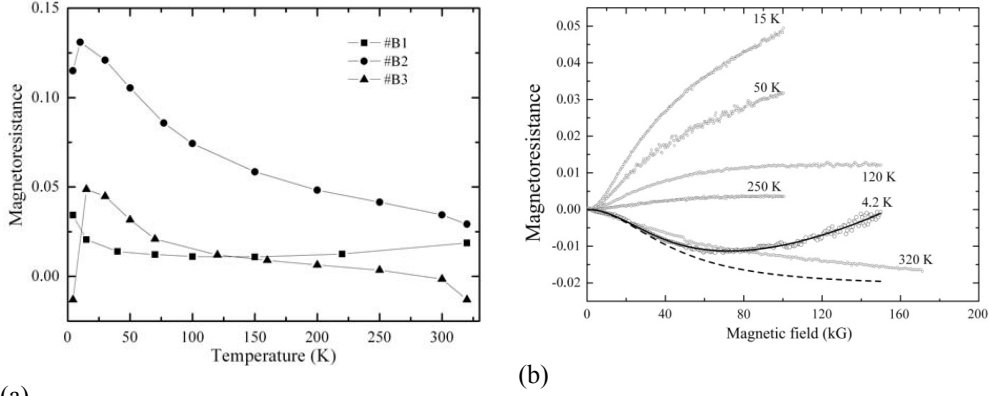


Fig. 25. Temperature dependence of the matrix magnetization for InMnSb sample #A2 (a) and sample #A4 (b). The contribution of the MnSb grains is subtracted. M_{PM} data (closed squares) are obtained from magnetization measurements. M_{eff} (open circles) is calculated from the results of magnetoresistance measurements under assumption that $\frac{\Delta\rho}{\rho}$ is proportional to the magnetization M for ferromagnetic state, and to M^2 for paramagnetic state, respectively. For sample #A4 circles deviate from the extrapolation of paramagnetic behavior to the higher M values demonstrating the transition to the ferromagnetic state [publication 6].

II-IV-As₂:Mn

Magnetoresistance measurements showed that the undoped sample #B1 ($Zn_{0.9}Cd_{0.1}GeAs_2$) had a positive magnetoresistance (up to 3.4% at 100 kG). Fig. 26a shows magnetoresistance versus temperature for manganese doped samples. Sample #B3 had small negative magnetoresistance (-1.5%) at $T=4.2$ K. At 5–7 K, magnetoresistance changed its sign, reached a maximum (~9%), and then decreased with increasing temperature. In temperatures from 15 to 250 K the $\frac{\Delta\rho}{\rho}(B)$ (Fig. 26b) can be described by a classical model for positive magnetoresistance [114] when two types of noninteracting carriers are present. Furthermore, the shapes of the temperature dependences of the ratio $\frac{\Delta\rho}{\rho}$ (Fig. 26a) for Mn-doped samples above 15 K are close to those of epitaxially grown MnAs with two types of carriers [115]. Above 300 K the sample #B3 showed an inflection toward negative values. This is characteristic of MnAs and accompanies the phase transition from the ferromagnetic hexagonal phase to the paramagnetic orthorhombic one [115]. At $T=4$ K, the $\frac{\Delta\rho}{\rho}(B)$ curve of the sample #B3 resemble the dependence observed for the dominant charge carrier scattering on isolated Mn ions outside magnetically ordered domains [112], because the magnetoresistance can be represented as the sum of two terms. The first term



(a) Fig. 26. Magnetoresistance vs. temperature for $Zn_{0.9}Cd_{0.1}GeAs_2$ samples at $B = 100$ kG (a) and vs. field for sample #B3 measured at different temperatures (b) [publication 2]. The solid line in (b) corresponds to the best fitting parameters at $T = 4.2$ K. The dashed line in (b) represents the negative term (Eq. 13). The solid lines in (a) are guide for eye.

$\left(\frac{\Delta\rho}{\rho}\right)_N$, according to Eq. 13, is proportional to $\langle S_z \rangle^2$, is dominating at $B < 70$ kG, and has a negative sign. The second term $\left(\frac{\Delta\rho}{\rho}\right)_P$ observed at $B > 70$ kG, is positive and has a classical quadratic dependence on the magnetic field. At high magnetic field the positive term is dominating. This gives possibility to separate the $\frac{\Delta\rho}{\rho}(T)$ to positive and negative terms.

$\frac{J_{pd}}{V} = 0.064$ and $T^* = 1.5$ K were found by fitting $\left(\frac{\Delta\rho}{\rho}\right)_N$ to Eq. 13 (Fig. 26b). A simple mean field theory [112] predict T^* very close to T_C . This points out the possibility of low – temperature FM ordering due to coupling of Mn moments in sample #B3. Therefore the mechanism of ferromagnetism in heavily Mn doped Mn $Zn_{0.9}Cd_{0.1}GeAs_2$ and InSb is the same.

4.4 Hall effect

InMnSb

The Hall resistivity of ferromagnets can be expressed by a sum of two terms,

$$\rho_H = R_0 B + R_S M = \rho_{OH} + \rho_{AH}, \quad (14)$$

where R_0 and R_S are the normal and the anomalous Hall coefficients, respectively. The normal Hall resistivity ρ_{OH} is caused by Lorenz force on charge carriers. The anomalous part ρ_{AH} is

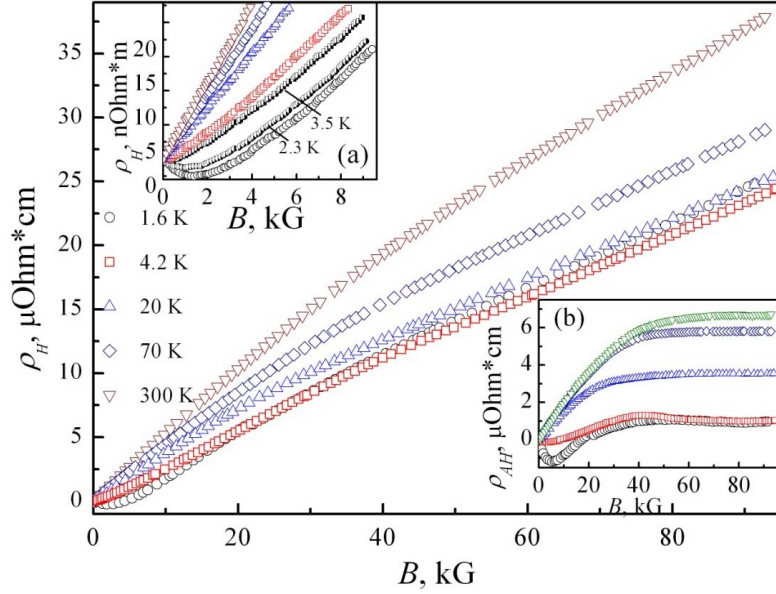


Fig. 27. Hall resistivity ρ_H of sample #B2 measured at various temperatures in fields up to $B = 95$ kG. Inset (a) illustrates the dependences of the low-field part of the Hall resistivity on magnetic field at different temperatures. Inset (b) presents the field dependences of the anomalous Hall resistivity ρ_{AH} at various temperatures. [publication 6]

proportional to M and in ferromagnetic materials it saturates in high magnetic fields. The anomalous Hall coefficient depends on the longitudinal resistivity as

$$R_S \propto \rho^n, \quad (15)$$

where $n = 1$ in the case of skew-scattering and $n = 2$ for the side-jump scattering and the intrinsic (Berry phase) mechanism [13]. We get $\rho_{AH}(B)$ by subtracting the contribution $\rho_{OH}(B)$ (which is very close to linear for $\text{In}_{1-x}\text{Mn}_x\text{Sb}$ [92]) from the total Hall resistivity ρ_H . In our InMnSb samples R_S is negative at $T < 10$ K and $B \sim 1$ kG. Note that in this sample the anomalous Hall effect (AHE) is observed even with small Mn content and when the $\rho(T)$ dependence (#A2 in Fig. 21) does not demonstrate the peak related to FM transition at low temperatures. The behavior of $\rho_{AH}(B)$ is nonmonotonic at low temperatures and similar to that observed $\text{In}_{1-x}\text{Mn}_x\text{Sb}$ epitaxial films [92]. As shown in the inset (a) of Fig. 27, R_S is negative in sample #B2 at low temperatures in weak magnetic fields and the anomalous Hall effect (AHE) is predominant ($R_S > R_0$). In high fields $\rho_H(B)$ is linear due to a shallow minimum and reversal of the sign below 40 kG and saturation in high magnetic fields. This may be explained within Berry-phase theory by a field-dependent relative shift of the heavy and light hole valence bands and the split off band [92].

However, such behavior (negative derivative of $\rho_{AH}(H)$ at low temperatures and small fields) could be related also to quantum corrections of conductivity [111], which is natural for such conditions.

Temperature dependences $M(T)$ is opposite to $\rho_H(T)$. Magnetization is decreasing and ρ_H is increasing with increasing of temperature. This could be due to increase of the carrier concentration, or due to crossover from hopping conductivity to conductivity along the percolation pass. This is seen also from Eq. (15) because ρ increases with increasing of temperature (see Fig. 20). AHE saturates at magnetic field which exceed the saturation field of magnetization by one order of magnitude. This is due to shape anisotropy of the sample because AHE measurements were performed in fields perpendicular to the sample plane while magnetization was measured in fields oriented along the sample. At higher temperatures classical relation $\rho_{AH} \sim M$ is not realize (see inset (b) in Fig. 27). The $\rho_{AH}(B)$ increases when the magnetic order in the InMnSb matrix vanishes. Both positive R_S and the saturation field of $\rho_{AH}(B)$ increase with increasing temperature. This points out on the increasing role of MnSb clusters in magnetic scattering of carriers. This is the additional source of ferromagnetism in InMnSb samples.

5 Conclusions

Mn-doped InSb and II-IV-As₂ semiconductors were synthesized by different methods. The structural, magnetic and electrical properties have been presented and analyzed in this work. These materials had many similar properties: the anomalous Hall effect up to room temperature, superparamagnetism at zero field and FM under magnetic field at temperatures close to Curie temperatures of MnSb (585 K) and MnAs (317 K) for InMnSb and II-IV-As₂:Mn, respectively. Negative magnetoresistance was observed at low temperatures and it was connected with scattering of spin-polarized carriers on Mn²⁺ ions. From presented results we can conclude that the following inclusions contribute to magnetization and magnetotransport in InMnSb and II-IV-As₂:Mn:

- MnX clusters are responsible for high temperature behavior of magnetization, positive magnetoresistance and Hall effect. These inclusions have inhomogeneous spatial distribution, sizes about hundreds nanometers and they have high Curie temperature. In InMnSb samples inclusions consisted from MnSb grains with nanometers size;
- MnAs nanoclusters with most probable radius about 3 – 5 nm are respond for low-field properties of samples;
- Mn complexes are responsible for the paramagnetic background and for FM transition in matrix at low temperatures. Mn complexes are mainly dimmers formed from Mn ions, substituting cation positions in the InSb and II-IV-As₂ matrix. The Mn solubility in the InSb matrix in this case is three times more than concentration of Mn complexes. However only small part (about 1/4) of Mn ions and complexes are located in the In sites contribute to the low temperature FM state.

In bulk crystals the majority of Mn atoms are located in MnX nanoclusters. This fact indicate that the high temperature ferromagnetism in Mn-doped InSb and II-IV-As₂ is due to MnX clusters. Analysis of the temperature and magnetic field dependencies of the resistivity, anomalous Hall coefficient and the magnetoresistivity shows that the ferromagnetic MnX nanoclusters and Mn ions influence significantly the charge transport in the investigated materials.

Further development of the research direction elaborated in this work suggest investigations of the monocrystalline magnetic hybrid materials based on InSb and II-IV-As₂. Magnetic wires are promising material for spintronics and its incorporating to diluted semiconductor matrix is perspective way to fabricate new two-phase magnetic systems. An example of such system is the directly solidified InSb-MnSb eutectic alloys. To grow

monocrystals with high carrier mobility is possible by using degrees of freedom associated with inherent shape anisotropy of MnSb wires.

The results obtained in this work may be useful for investigations of other III-V and II-IV-V₂ semiconductors doped with 3d elements, containing nanoclusters, especially materials which are expected to exhibit above room temperature ferromagnetism.

References

1. Zutic I, Fabian J and Das Sarma S 2004 *Rev. Modern. Phys.* **76** 323.
2. Huang B, Monsma D J, Appelbaum I 2007 *Phys. Rev. Lett.* **99** 177209.
3. Ando K 2006 *Science* **312** 1883.
4. Ohno H 1998 *Science* **281** 951.
5. Ivanov V A, Aminov T G, Novotortsev V M and Kalinnikov V T 2004 *Russian Chemical Bulletin* **53** 2357.
6. Gulyaev Yu V, Zilberman P E, Panas A I, and Epshtein E M 2009 *Phys. Usp.* **52** 335.
7. Fert A 2008 *Phys. Usp.* **51** 1336.
8. Prinz G A 1998 *Science* **282** 1660.
9. Awschalom D D, and Flatte M E 2007 *Nature Physics* **3** 153.
10. Koo H C, Kwon J H, Eom J, Chang J, Yan S H, and Johnson M 2009 *Science* **325** 1515.
11. Wunderlich J, Park B.-G., Zbrbo L P, Rozkotov E, Nemeč P, Novak V, Sinova J, and Jungwirth T 2010 *Science* **330** 1801.
12. Novak V, Olejnik K, Wunderlich J, Cukr M, Viborni K, Rushforth A W, Edmonds K W, Champion R P, Gallagher B L, Sinova J, and Jungwirth T 2008 *Science* **330** 1801.
13. Jungwirth T, Sinova J, Mašek J, Kučera J, MacDonald A H 2006 *Rev. Modern. Phys.* **78** 809.
14. Macdonald A H, Schiffer P, and Samarth N 2005 *Nature Materials* **4** 195.
15. Sawicki M, Chiba D, Korbecka A, Nishitani Y, Majewski J A, Matsukura F, Dietl T, and Ohno H 2009 *Nat. Phys.* **6** 22.
16. Chiba D, Sawicki M, Nishitani Y, Nakatani Y, Matsukura F, and Ohno H 2008 *Nature* **455** 515.
17. Ohno Y, Young D K, Beschoten B, Matsukura F, Ohno H, and Awschalom D D 1999 *Nature* **4025** 790.
18. Tanaka M, and Higo Y 2001 *Phys. Rev. Lett.* **87** 026602.
19. Chiba D, Sato Y, Kita T, Matsukura F, and Ohno H 2004 *Phys. Rev. Lett.* **93** 216602.
20. Olejnik K, Owen M H S, Novak V, Mašek J, Irvine A C, Wunderlich J, and Jungwirth T 2008 *Phys. Rev. B* **78** 054403.
21. Wang M, Champion R P, Rushforth A W, Edmonds K W, Foxon C T, and Gallagher B L 2008 *Appl. Phys. Lett.* **93** 132103.
22. Novak V, Olejnik K, Wunderlich J, Cukr M, Viborni K, Rushforth A W, Edmonds K W, Champion R P, Gallagher B L, Sinova J, and Jungwirth T 2008 *Phys. Rev. Lett.* **101** 077201.

23. Chen L, Yang X, Yang F, Zhao J, Misuraca J, Xiong P, and von Molnar S 2011 *Nano Lett.* **11** 2584.
24. Brudnyi V N 2009 *Semiconductors* **43** 1146.
25. Shay J L, and Wernic J H 1975 *Chalcopyrite semiconductors: Growth, Electronic properties and Applications* (Pergamon, New York).
26. 1974 $A^{II} - B^{IV} - C$ *Semiconductors*, Ed by N.A. Goryunova, Yu. A. Rud', and Yu. A. Valov (Sov. Radio, Moscow).
27. Medvedkin G A 2002 *Technical Physics Letters* **28** 889.
28. Erwin S C and Tutiz I 2004 *Nature Materials* **3** 410.
29. Sato K, Medvedkin G A, Nishi T, Hasegawa Y, Misawa R, Hirose K, and Ishibashi T 2001 *J. Appl. Phys.* **89** 7027.
30. Medvedkin G A, Baranov P G, Goloshapov S I 2003 *J. Phys. Chem. Sol.* **64** 1691.
31. Medvedkin G A, Ishibashi T, Nishi T, and Sato K 2001 *Semiconductors* **35** 291.
32. Novotortsev V M, Marenkin S F, Varnavskii S A, Koroleva L I, Kupriyanova T A, Szymczak R, Kilanski L, and Krzymanska B 2008 *Russ. J. Inorg. Chem.* **53** 22.
33. Demin R V, Koroleva L I, Marenkin S F, Mikhailov S G, Novotortsev V M, Kalinnikov V T, Aminov T G, Szymczak R, Szymczak H, and Baran M 2004 *Technical Physics Letters* **30** 924.
34. Asubar J T, Jinbo Y, and Uchitomi N 2009 *J. Cryst. Growth.* **311** 929.
35. Aitken J A, Tsoi G M, Wenger L E, and Brock S L 2007 *Chem.Mater.* **19** 5272.
36. Pearton S J, Overberg M E, Abernathy C R, Theodoropoulou N A, Hebard A F, Chu S N G, Osinsky A, Fuflyigin V, Zhu L D, Polyakov A Y, and Wilson R G 2002 *J. Appl.Phys* **92** 2047.
37. Koroleva L I, Pavlov V Yu, Zashchirinskiĭ D M, Marenkin S F, Szymczak R, Varnavsky S A, Dobrowolski W, and Kilanski L 2007 *Physics of the Solid State* **49** 2121.
38. Vurgaftman I, and Meyer J R 2004 *Phys. Rev. B* **69** 115203.
39. Kawakami R K, Johnston-Halperin E, Chen L F, Hanson M, Guebels N, Speck J S, Gossard A C, and Awschalom D D 2000 *Appl. Phys. Lett.* **77** 3665.
40. Tagaki Y, Lihnemann J, Jenichen B, Herfort J, Hermann C, and Jahn U 2010 *Appl. Phys. Lett.* **108** 123510.
41. Chen X, Na M, Cheon M, Wang S, Luo H, McCombe B D, Liu X, Sasaki Y, Wojtowicz T, Furdyna J K, Potashnik S J, and Schiffer P. 2002 *Appl. Phys. Lett.* **81** 511.
42. Wang K Y, Sawicki M, Edmonds K W, Champion R P, Rushforth A W, Freeman A A, Foxon C T, Gallagher B L, and Dietl T 2006 *Appl. Phys. Lett.* **88** 022510.

43. Michel C, Elm M T, Goldłbcke B, Baranovskii S D, Thomas P, Heimbrodt W, and Klar P J 2008 *Appl. Phys. Lett.* **92** 223119.
44. Elm M T, Michel C, Stehr J, Hofmann D M, Klar P J, Ito S, Hara S, and Krug von Nidda H-A 2010 *J. Appl. Phys.* **107** 013701.
45. Lawniczak-Jablonska K, Wolska A, Bak-Misiuk J, Dynowska E, Romanowski P, Domagala J Z, Minikayev R, Wasik D, Klepka M T, Sadowski J, Barcz A, Dluzewski P, Kret S, Twardowski A, Kaminska M, Persson A, Arvanitis D, Holub-Krappe E, and Kwiatkowski A 2009 *J. Appl. Phys.* **106** 083524.
46. Ivanov V A, Pashkova O N, Ugolkova E A, Sanygin V P, and Galera R M 2008 *Inorganic Materials* **44** 1041.
47. Sanygin V P, Pashkova O N, and V A Ivanov 2008 *Inorganic Materials* **44** 1285.
48. Sanygin V P, Pashkova O N, Filatov A V, and Novotortsev V M 2010 *Inorganic Materials* **46** 807.
49. Ganesan K, Mariyappan S, and Bhat H L 2007 *Solid State Communications* **143** 272.
50. Ganesan K, and Bhat H L 2008 *J. Appl. Phys.* **103** 043701.
51. Teramoto I, and Van Run A M J G 1968 *J. Phys. Chem. Sol.* **29** 347.
52. Hatfield S A, Bell G R 2006 *J. Cryst. Growth.* **296** 165.
53. Abe E, Matsukura F, Yasuda H, Ohno Y, and Ohno H 2000 *Physica E* **7** 981.
54. Han G C, Ong C K, and Liew T Y F 1999 *J. Magn. Magn. Mat.* **192** 233.
55. Braun W, Trampert A, Kaganer V M, Jenichen B, Satapathy D K, and Ploog K H 2006 *J Cryst. Growth* **301-302** 50.
56. Akinaga H, and Mizuguchi M 2000 *Appl. Phys. Lett.* **76** 2600.
57. Zhang H, Kushvaha S S, Chen S, Gao X, Qi D, Wee A T S, and Wang X S. 2007 *Appl. Phys. Lett.* **90** 202503.
58. Size S M 1981 *Physics of Semiconductor Devices* (2nd ed., John Wiley & Sons, New York).
59. Wei C Y, Wang K L, Taft E A, Swab J M, Gibbons M D, Davern W E, and Brown D M 1980 *IEEE Trans. Electron Devices* **27** 170.
60. Ashley T, Dean A B, Elliott C T, Pryce G J, Johnson A D, and Willis H 1995 *Appl. Phys. Lett.* **66** 481.
61. Liu W E, and Mohny S E 2003 *Mat. Sci. Eng. B* **103** 189.
62. Obukhov S A, Neganov B S, Kiselev Yu F, Chernikov A N, Vekshina V S, Pepik N I, and Popkov A N 1991 *Cryogenics* **31** 874.
63. Dashevskii M Y, Ivleva V S, Krol L Y, Kurilenko I N, Litvak-Gorskaya L B, Mitrofanova R S, and Fridlyand E Y 1971 *Sov. Phys. Semicond.* **5** 757.

64. Teubert J, Obukhov S A, Klar P J, and Heimbrodt W 2009 *Phys. Rev. Lett.* **102** 046404.
65. Partin D L, Heremans J, and Thrush C M 1997 *J. Cryst. Growth.* **175/176** 860.
66. Wojtowicz T, Cywieski G, Lim W L, Liu X, Dobrowolska M, Furduna J K, Yu K M, Walukiewicz W, Kim G B, Cheon M, Chen X, Wang S M, and Luo H 2003 *Appl. Phys. Lett.* **82** 4310.
67. Wojtowicz T, Lim W L, Liu X, Cywieski G, Kutrowski M, Titova L V, Yee K, Dobrowolska M, Furduna J K, Yu K M, Walukiewicz W, Kim G B, Cheon M, Chen X, Wang S M, Luo H, Vurgaftman I, and Meyer J R 2003 *Physica E* **20** 325.
68. Yanagi S, Kuga K, Slupinski T, and Munekata H 2004 *Physica E* **20** 333.
69. Hollingsworth J, and Bandaru P R 2008 *Materials Science and Engineering B* **151** 152.
70. Danilov Yu A, Demidov E S, Drosdov Yu N, Lesnikov V P, Podolski V V, Sapozhnikov M V, and Kasatkin A P 2006 *J. Magn. Magn. Mater.* **300** e24.
71. Parashar N D, Rangaraju N, Lazarov V K, Xie S, and Wessels B W 2010 *Phys Rev B.* **81** 115321.
72. Peters J A, Rangaraju N, Feeser C, and Wessels B W 2011 *Appl. Phys. Lett.* **98** 193506.
73. Rednic L., Deac I. G., Dorolti E., Coldea M., Rednic V., and Neumann M. 2010 *Central European Journal of Physics* **8** 620.
74. Chen T., Charlan G.B., and Keezer R.C., 1977 *J. Cryst. Growth.* **37** 29.
75. Varnavskii S. A., Shabunina G.G., and Trukhan V.M. 2007 "Topical Problems of Solid State Physics", Collected Works (Minsk). **2**. 126.
76. Vaipolin A.A., Osmanov E.O., and Prochukhan V.D. 1972 *Izv. Akad. Nauk SSSR, Neorg. Mater.* **8**. 947.
77. Dean J.A., 1999 *Lange`s Handbook of Chemistry* 15th edn (New York: McGraw-Hill) pp.4.30-4.
78. Novotortsev V.M., Palkina K.K., Mikhailov S.G., Molchanov A.V., Ochertynova L.I., and Marekin S.F. 2005 *Inorganic Materials* **41** 439.
79. Novotortsev V.M., Kochura A.V., and Marenkin S.F. 2010 *Inorganic Materials* **46** 19.
80. Pytlik L., and Zieba A. 1985 *J. Magn.Magn.Mater.* **51** 1999.
81. De Blois R.W., Rodbell D.S. 1963 *J.Appl.Phys.* **34** 1101.
82. Okita T and Makino Y. 1968 *J. Phys. Soc. Japan* **25** 120.
83. Takei W.J., Cox D.E., and Shirane G. 1963 *Phys. Rev.* **129** 2008.
84. Prasad S., Gajbhiye N.S. 1998 *J. Alloys and Compounds* **265** 87.
85. Stoner E.C., Wohlfarth E.P. 1948 *Phil. Trans. Roy. Soc. A* **240** 599.
86. Demin R., Koroleva L., Marenkin S., Mikhailov S., Aminov T., Szymczak H., Szymczak R., and Baran M. 2005 *J. Magn. Magn. Mater.* **290 - 291** 1379.

87. Novotortsev V.M., Kalinnikov V.T., Koroleva L.I., Demin R.V., Marenkin S.F., Aminov T.G., Shabunina G.G., Boijchuk S.V., and Ivanov V.A. 2005. *Russ. J. Inorg. Chem.* **50** 492.
88. Raebiger H., Ayuela A., and von Boehm J. 2005 *Phys. Rev. B.* **72** 014465.
89. Soo Y. L., Kim S., Kao Y. H., Blattner A. J., Wessels B. W., Khalid S., Sanchez Hanke C., and Kao C. C. 2004 *Appl.Phys. Lett.* **84** 481.
90. Jaeger C., Bihler C., Valliatis T., Coennenwein S. T. B., Opel M., Gross R., and Brandt M. S. 2006 *Phys. Rev. B.* **74** 045330.
91. Sanvito S., and Hill N.A. 2000 *Phys. Rev. B* **62** 15553.
92. Mihaly G., Csontos M., Bordacs S., Kezsmarki I., Wojtowicz T., Liu X., Janko B., and Furduna J. K. 2008 *Phys. Rev. Lett.* **100** 107201.
93. Laiho R., Lisunov K.G., Lähderanta E., and Zakhvalinskii V.S. 1999 *J. Phys.:Cond. Matter.* **11** 555.
94. Bean C.P., and Livingstone J.D. 1959 *J. Appl. Phys.* **30** S120.
95. Menyuk N., Kafalas J.A., Dwight K, and Goodenough J.B. 1969 *Phys.Rev.* **177** 942.
96. Koroleva L.I., Zashirinskii D.M., Khapaeva T.M., Marenkin S.F., Fedorchenko I.V., Szymczak R., Krzumanska B., Dobrovolskii V., and Kilanskii L. 2009 *Physics of the Solid State* 51 303.
97. Low B. L., Ong C. K., Lim J., Huan A. C. H., Gong H., and Liew T. Y. F. 1999 *J.Appl.Phys.* **85** 7340.
98. Heimbrodt W., Klar P.J., Ye S., Lampalzer M, Michel C., Baranovskii S.D., Thomas P., and Stolz W. 2005 *J. Supercond.* **18** 315.
99. Aronzon B.A., Kapelnitsky S.V., and Lagutin A.S. 2007 Transport and magnetic properties of nanogranular metals *Physico-Chemical Phenomena in Thin Films and at Solid Surfaces (Thin Films and Nanostructures)* vol. 34 ed. L. I. Trakhtenberg et al (Oxford: Academic Press) pp 582 – 633.
100. Zvyagin I.P., and Keiper R. 2002 *Phys. Status Solidi (b)* **230** 151.
101. Sinova J., Jungwirth T., and Cerne J. 2004 *International Journal of Modern Physics B* **18** 1083.
102. Csontos M., Mihaly G., and Janko B. Wojtowicz T., Liu X., Furduna J. K. 2005 *Nature Materials* **4** 447.
103. Zarand G., Moca C.P., and Janko B. 2005 *Phys.Rev.Lett.* **94** 247202.
104. Timm C. J.2003 *J. Phys.: Condens. Matter* **15** R1865.
105. Yuldashev Sh. U., Jeon H. C., Im H. S., Kang T. W., Lee S. H., and Fudyna J. K. 2004 *Phys. Rev. B* **70** 193203.

106. Aronzon B. A., Pankov M. A., Rylkov V. V., Meilikhov E. Z., Lagutin A. S., Pashaev E. M., Chuev M. A., Kvardakov V. V., Likhachev I. A., Vihrova O. V., Lashkul A. V., Lähderanta E., Vedeneev A. S., and Kervalishvili P. 2010 *J. Appl. Phys.* **107** 023905.
107. Li A.P., Shen J., Thompson J. R., and Weitering H. H. 2005 *Appl. Phys. Lett.* **86** 152507.
108. Kaminski A., and Das Sarma S. 2003 *Phys. Rev. B* **68** 235210.
109. Gudenko S.V., Aronzon B.A., and Ivanov V.A. 2005 *Pisma Zh. Eksp. Fiz.* **82** 591.
110. Aronzon B.A 2008 *HAIT J. Sci. Eng. A* 5 52.
111. Lee P. A., and Ramakrishnan T. V. 1985 *Rev. Mod. Phys.* **57** 287.
112. Csontos M., Wojtowicz T., Liu X., Dobrowolska M., Janky B., Furduna J.K., and Mihály G. 2005 *Phys. Rev. Lett.* **95** 227203.
113. Bñal-Monod M.-T., and Weiner R.A. 1968 *Phys. Rev.* **170** 552.
114. Ziman J.M. 1960 *Electrons and Phonons* (Oxford: Oxford University Press).
115. Mira J., Rivadulla F., Rivas J., Fondado A., Guidi T., Caciuffo R., Carsughi F., Radaelli P.G., and Goodenough J.B. 2003 *Phys. Rev. Lett.* **90** 97203.